It's just a phase: high-contrast imaging with patterned liquid-crystal phase plates to facilitate characterization of exoplanets

Doelman, D.S.

Citation

Doelman, D. S. (2021, June 22). *It's just a phase: high-contrast imaging with patterned liquid-crystal phase plates to facilitate characterization of exoplanets*. Retrieved from https://hdl.handle.net/1887/3191978

Author: Doelman, D.S.
Title: It's just a phase: high-contrast imaging with patterned liquid-crystal phase plates to facilitate characterization of exoplanets
Issue Date: 2021-06-22

1 Introduction

"For then why may not every one of these Stars or Suns have as great a Retinue as our Sun, of Planets, with their Moons, to wait upon them?" - Christiaan Huygens, Cosmotheoros

Christiaan Huygens (1629-1695) was a brilliant Dutch scientist and is well known for his work in the field of mathematics, physics, and astronomy. He also had an aptitude for instrumentation, building telescopes together with his brother, which he used to discover Saturn's moon Titan, and showing with observations that Saturn?s rings were in fact, rings. His final work *Cosmotheoros* had a more philosophical nature, where he, like many before and after him, wondered about the existence of planets around other stars. The idea of planets existing around other stars was not unheard of after the publications of Giordano Bruno (1584), however, what sets him apart is the idea to use telescopes to detect these planets. *"For let us fancy our selves placed at an equal distance from the Sun and fix'd Stars; we should then perceive no difference between them. For, as for all the Planets that we now see attend the Sun, we should not have the least glimpse of them, either that their Light would be too weak to affect us, or that all the Orbs in which they move would make up one lucid point with the Sun."* Huygens (1698), translation by Timothy Childe. It is likely that from his work on the distance between the Earth and the Sun and by comparing the brightness of Sirius with the Sun, he knew that these planets would be extremely close in angular separation and that detecting them would be difficult, if not impossible. Many after Christiaan Huygens have sought to prove the theory that planets exist around other star, yet it was not until 1992 that the first extra-solar planets were discovered by Wolszczan & Frail (1992). These planets were approximately four times the mass of the Earth, and orbited a pulsar which is the remnant of a supernova. Wolszczan and Frail used arrival time variations of radio waves emitted by the pulsar to infer the existence of these two planets. We note that with Christiaan Huygens' prediction, it is perhaps not surprising that these first exoplanets have been discovered through indirect detection.

These two planets provided a first look into the diversity in planets, as they orbited a stellar remnant and with their masses they had no counterpart in the solar system. A second clue that our solar system is not a standard system was given by the detection of Pegasi 51 b, a gas giant orbiting extremely close to the host star (Mayor & Queloz, 1995). Such planets are massive enough to significantly to make the star 'wobble' around their common center of mass. Using the Doppler effect, the radial velocity (RV) of these stellar movements can be measured and the existence of exoplanets inferred. This method was used by Mayor and Queloz to determine the mass of Pegasi 51 b (0.47 M_J) and the orbital period of 4.2 days. Jovian planets orbiting so close to their host star absorb a lot of stellar flux, which heats them to extreme temperatures ($>$ 1000 K), resulting in their classification as hot Jupiters. It was realized that this type of planet would have a significant chance of passing in front of their star, partially obscuring them. Measuring the flux decrease of a host star when a planet passes in front is a third indirect method[1]

---

[1] If this method is purely indirect can be debated. The atmosphere of the planet leaves a

of exoplanet detection and is called the transit method. The extinction ratio of the stellar flux gives a measure of the planetary radius, and the first planet detected with this method is HD 209458 b (Charbonneau et al., 2000; Henry et al., 2000) with a radius of 1.27 R_J and an orbital period of 3.52 days, similar to Pegasi 51 b. HD 209458 b was also detected with the RV method, resulting in a mass estimate of 0.62 M_J (Henry et al., 2000). Interestingly, the density is much lower than that of Jupiter, showing that it is inflated due to the extreme temperature of the planet.

Probing the full exoplanet population is difficult due to intrinsic biases of the aforementioned detection methods. The RV and the transit method are most sensitive to massive planets orbiting close to the star and in the line of sight of the observer. A fourth indirect detection method uses precise astrometry to measure the wobble of a star and it alleviates the line of sight bias. It is particularly sensitive to planets orbiting in a face-on orbit, making it complementary to the RV and transit method. The *Gaia* satellite is capable of precise astrometry and current estimates indicate that it will find 21,000 exoplanets in a 5 year period (Perryman et al., 2014). The *Gaia* results are expected soon. However, indirect measurements are still biased towards close-in planets and provide little more information than the orbit, mass and radius. Measuring the bulk composition does not constrain anything about the atmosphere, which makes up only a small fraction of the mass and radius of a planet. Understanding the atmosphere is important for distinguishing between a Venus-like and Earth-like exoplanet, and in the end determining the habitability of an exoplanet. *Cosmotheoros* is a famous example on how misconceptions about planetary atmospheres can lead to wrong conclusions on habitability. Christiaan Huygens philosophized that other planets in the solar system were inhabited like Earth, because they too would have the most important ingredient for life: liquid water. He based this assumption on the observation that Jupiter has dark spots which he identified as clouds, and, that if Earth and Jupiter had water and clouds, so would the other planets. Interestingly, Huygens identified the problem that water on Earth would freeze on the outer planets and evaporate on the inner planets, but rather than defining a habitable zone, he proposed a change in water properties on the other planets[2]. Today we recognize that even finding an Earth sized planet in the habitable zone of a star does not mean that it can or does harbor life. In order to answer the fundamental question if we are alone in the universe, we first must understand the many processes involved in planet formation and evolution, as well as have a good understanding of atmospherical and geological processes (Snellen et al., 2019).

---

spectral imprint and extremely hot planets also can be detected in emission. See section 1.1.

[2] "Every Planet therefore must have its Waters of such a temper, as to be proportion'd to its heat: Jupiter's and Saturn's must be of such a nature as not to be liable to Frost; and Venus's and Mercury's of such, as not to be easily evaporated by the Sun. " - Huygens (1698)

1.1 The era of exoplanet characterization

Exoplanet research aims to understand the place of Earth and the Solar System in the universe. During the last three decades the number of detected exoplanets has rapidly grown to over 4300 exoplanets [3]. For a significant fraction of these planets we know the their bulk-composition through a comparison between the measured densities and models for rocky planets or gaseous planets (Howard et al., 2013). From the bulk composition we can infer that there are different types of planets that were not present in our solar-system, e.g. mini-Neptunes or super-Earths (Petigura et al., 2013) This gave us already a more complete picture of the planet population, and statistical properties of the population as a whole become unique constraints on planet formation models (Benz et al., 2014). Moreover, we learned that rocky planets are very common, and the chances of an Earth analogue orbiting a nearby star are high. However, if we are to understand how unique Earth, and the life on Earth truly is, it is critical that we gain a more detailed understanding of the exoplanet population and especially their atmospheres.

1.1.1 Methods of exoplanet characterization

Two techniques have successfully demonstrated being capable of characterizing exoplanet atmospheres, transit spectroscopy and direct imaging. Low-resolution transit spectroscopy measures the transit depth variations as function of wavelength caused by the atmospheric constituents changing the opacity of the atmosphere. Hot Jupiters are prime targets for transit spectroscopy due to their size and distance to the star. Accurately measuring the transit depth as function of wavelength has revealed the existence of clouds and hazes in hot Jupiters (Sing et al., 2016). Extending the observations to the full phase curve with emission spectroscopy, the vertical and longitudinal, thermal structure of the atmosphere of WASP-43 was resolved (Stevenson et al., 2014). A similar effort for lower-mass planets revealed that finding molecular features using transit spectroscopy is hindered by the presence of clouds (Kreidberg et al., 2014). With high-resolution spectroscopy (HRS) it is possible to measure the Doppler shift of planetary atomic lines during the transit. Exploiting this shift revealed neutral iron and ionized atomic iron and titanium (Fe^+ and Ti^+) in the hot Jupiter Kelt-9b (Hoeijmakers et al., 2018b). High-resolution spectroscopy can also be used to detect Doppler-shifted emission and absorption features from hot Jupiters during the full phase curve (Snellen et al., 2010).

With direct imaging the planet is spatially resolved from the star, enabling the direct measurement of planet light that is reflected and/or thermal. HRS combined with direct imaging and optical stellar suppression techniques (coronagraphs) provides additional suppression of stellar light and can be used to characterize planetary atmospheres (Wang et al., 2017). Moreover, HRS can be used to measure the Doppler shift of the planet light, which can be used to constrain the orbit

---

[3] `https://exoplanets.nasa.gov/` - Feb 16, 2021

and the linewidth is a measure for rotational broadening (Snellen et al., 2014). Direct imaging combined with medium-resolution spectroscopy cannot resolve the Doppler shift, however it still resolves spectral lines of molecular species not present in the stellar spectrum. This has been used to detect molecular species like water and carbon monoxide and the accretion tracer Hα in young giant exoplanets at large separations (dit de la Roche et al., 2018; Hoeijmakers et al., 2018a; Haffert et al., 2019). Low-resolution spectroscopy is only sensitive to molecular bands, but is the most widely used form of spectroscopy for exoplanet characterization. So far this has lead to the detection of water, carbon monoxide and methane in young giant exoplanets (Konopacky et al., 2013a; Macintosh et al., 2015), and the combination is used to constrain the C/O ratio compared to their host star (Wang et al., 2020; Mollière et al., 2020). Moreover, polarimetric measurements of exoplanets could be used to determine oblateness or cloud coverage (Stolker et al., 2017), or even the formation history through the orientation of circumplanetary disks (van Holstein et al., 2021). Lastly, photometric monitoring of directly imaged exoplanets has been successful (Zhou et al., 2020), and could also provide more insight in the cloud coverage.

1.1.2 Direct imaging of HR 8799

To demonstrate what information can be extracted from directly imaged exoplanets, we summarize the results of the most studied system with direct imaging: HR 8799. HR 8799 A is a young (<100 Myr) A star at 39 parsec with a large debris disk (Su et al., 2009). The HR 8799 system hosts at least four giant planets which have been detected by Marois et al. (2008, 2010). The planets orbit at large separations, between 15 and 70 AU, and have masses around 7 $M_{\rm Jup}$, although this is age dependent. A selection of some of the results is shown in Fig. 9.2. Gas giants, like the HR 8799 planets, are thought to be similar to field brown dwarfs, as they have a similar radius, composition and slow cooling rate (Skemer et al., 2014). Field brown dwarfs are substellar objects with masses between 13 and 80 $M_{\rm Jup}$, which is not enough mass to trigger sustained nuclear fusion of hydrogen in their cores. Therefore, they slowly cool down after formation through thermally radiating the gravitational energy released during formation. The atmospheres of brown dwarfs (and gas giants) regulate this cooling and thus their evolution, and observing these atmospheres is essential for their characterization. Field brown dwarfs are more easily studied as they are not obscured by a much brighter host star, and many already have been found (Kirkpatrick et al., 2011) and characterized (Burgasser, 2014). As brown dwarfs are cooling they change spectral type due to changes in their atmospheres. One of these transitions is the L-T transition, where their atmospheres transition from CO-rich and cloudy (L-type), to CH_4-rich and relatively cloud free (T-type), e.g. Vos et al. (2019). For field brown dwarfs this happens for temperatures cooler than 1400K, over a narrow temperature range of $\sim$ 200K. During this period, the clouds are thought to sink below the photosphere and the near-IR color shifts toward the blue. Due to the similarities between gas giants and brown dwarfs, it is thought that gas giants also show this L-T transition. We

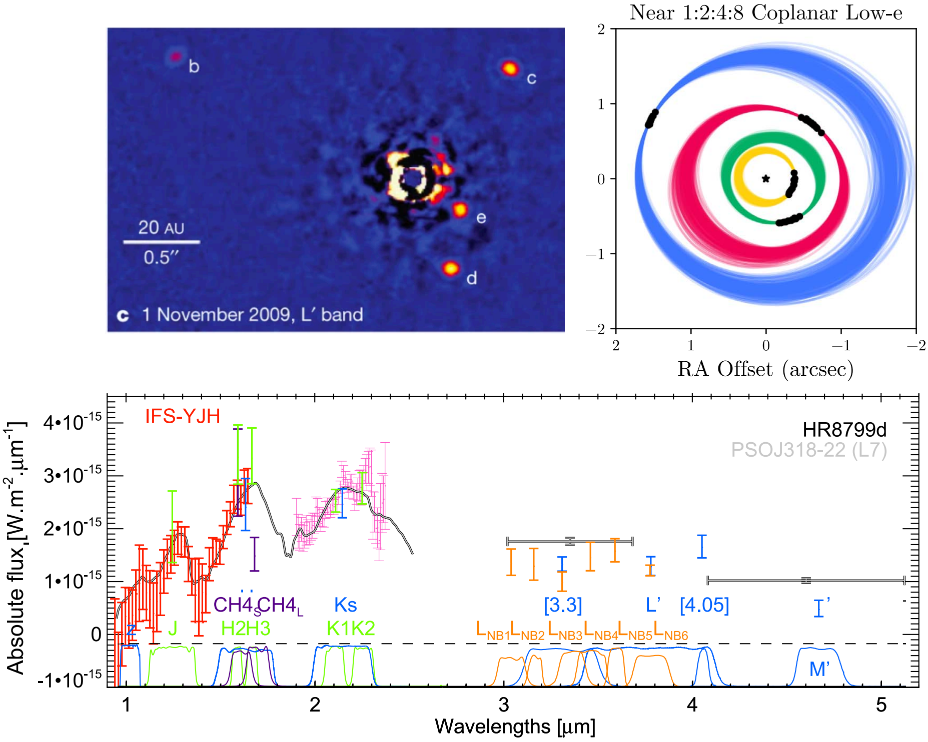

Figure 1.1: Selected results of studies on the HR 8799 system. *Top left:* Image of the HR 8799 planetary system, showing all four planetary companions. Adapted from Marois et al. (2010). *Top right:* Allowed orbits of the four planets, taking into account dynamical constraints. Adapted from Wang et al. (2018). *Bottom:* Comparison between the combined spectrum of planet d taken with multiple instruments and a field brown dwarf of type L7. Adapted from Bonnefoy et al. (2016).

note that the physical mechanism of the L-T transition in brown dwarfs is not yet fully understood (Vos et al., 2019). With the detection of the HR 8799 planets, it was shown that their location of the in a near-IR color-magnitude diagram was close to the L-T transition (Marois et al., 2008). Their temperatures (1100K) were closer to a T-type brown dwarf, while clouds were required to properly fit the photometric points, directly challenging the brown dwarf models. Medium resolution spectroscopy of HR 8799 b also showed no significant methane absorption, which would be expected for a T-type brown dwarf of similar absolute magnitude (Bowler et al., 2010). Using high-resolution spectra it was confirmed that HR 8799 b does contain water, methane and carbon monoxide (Konopacky et al., 2013b; Barman et al., 2015). New M band and L band photometry also suggested the presence of thick clouds and absence of CH_4 (Skemer et al., 2014; Currie et al., 2014). Overall, the early results showed significant differences between field brown dwarfs and their models, possibly as a consequence of the lower surface gravity (Marley et al., 2012). In addition, adaptations to the models resulted in exploration of carbon disequilibrium chemistry and uniform or patchy clouds (Bowler et al., 2010; Barman et al., 2011; Skemer et al., 2012).

New direct imaging instruments with low-resolution spectroscopic capabilities were used to get the first spectra of the HR 8799 planets (Oppenheimer et al., 2013; Zurlo et al., 2016; Greenbaum et al., 2018). These spectra were not fitted well with spectra of field brown dwarfs, although a better fit is realized by comparing with low-gravity brown dwarfs (Bonnefoy et al., 2016). Modelling the spectra to retrieve atmospheric parameters was partially successful by including thicker clouds compared to brown dwarfs. However, many different models only properly fit 1.1-2.5 μm or the thermal infrared (3-5 μm), not both simultaneously, e.g. (Barman et al., 2015; Bonnefoy et al., 2016). Attempts at characterizing the atmospheres therefore lead to different conclusions on cloud coverage (uniform vs patchy) (Mollière et al., 2020; Currie et al., 2014) and equilibrium vs. disequilibrium chemistry (Lavie et al., 2017; Mollière et al., 2020), depending on which part of the spectrum was prioritized. Recently, updated self-consistent models started to produce better results by taking into account the lower gravity, producing an increase of cloud optical depth (Charnay et al., 2018). Moreover, these models predict a greenhouse effect that shifts the carbon chemical equilibrium, changing the abundances of species compared to similar temperature brown dwarfs with higher surface gravity. These models do not (yet) include non-uniformity in cloud layers. However, is to be expected that in the transition from uniform clouds (L-type) to no clouds (T-type), patchy clouds can be an intermediate state. Another way of probing cloud patchiness is through photometric monitoring of planetary companions, which is already observed for brown dwarfs (Apai et al., 2017). It is found that many brown dwarfs (L- and T-type) are variable, but they vary most strongly during the L-T transition (Metchev et al., 2015). Measuring this variability for HR 8799 planets was attempted but sensitivity not good enough (Biller et al., 2021). Yet another method to probe cloud patchiness is through polarimetric observations. For planets with uniform clouds the linear polarization signal is expected to be zero, while patchy clouds could generate a linear polarization signal of up to 0.03% and 1.33%(Stolker et al., 2017). Measurements of linear polarization of the HR 8799 planets resulted in upper limits of $\sim 1\%$ (van Holstein et al., 2017, 2021). While this is a stringent upper limit, it does not constrain the cloud patchiness.

Other information from direct imaging comes from continuous monitoring of the HR 8799 system to track the orbits of the planets. These studies show that the planets are in near 1:2:4:8 resonance and from dynamical constraints it can be shown that the orbits are almost co-planar (Konopacky et al., 2016; Lacour et al., 2019). The resonances have implications on the planet formation, suggesting that they were locked in resonance quickly after formation, before the gaseous protoplanetary disk disappeared (Wang et al., 2018). However, it can not be used to probe the formation mechanism of the planets, and the uncertainty about the formation mechanism also results in different upper limits on the derived dynamical mass of the planets. A method that can be used to study the formation history of the HR 8799 planets requires a measurement of the planetary C/O ratio. Depending on the formation mechanism and formation location in the protoplanetary disk, the C/O ratio of the planet can be different to the stellar C/O ratio (**?**). The C/O ratios in the atmospheres of the HR 8799 planets are consistent with superstellar (Konopacky et al., 2013b; Barman et al., 2015; Mollière et al., 2020), although stellar C/O ratios are also not excluded due to degeneracies (Wang et al., 2020; Mollière et al., 2020). A superstellar C/O ratio could be indicative of planet formation beyond the CO snowline, the region in the disk with temperatures that make CO freeze onto grains, and planet migration (Mollière et al., 2020). Lastly, the interaction with the debris disk could also be used to find evidence of planet migration. The orbital fits of planet b at show that its location is consistent with sculpting the inner edge of the debris disk, favouring a more stable system (Wang et al., 2018). However, the debris disk has a large halo of small grains extending out to 1000 AU, possibly originating from unstable orbits or planet migration (Su et al., 2009).

To summarize, direct imaging has given a wealth of information about the HR 8799 system, which already provided tests for planet formation and evolution theories, as well as drive the exoplanet atmosphere model development. Up to now direct imaging has been limited to young, massive planets on wide orbits, yet it has the potential to provide the same revolution for a wider range of planets. In this thesis we will show the challenges of direct imaging and explore technological advancements that will help find lower mass exoplanets closer to their star.

1.2 Direct imaging systems

1.2.1 The challenge of direct imaging

The goal of direct imaging is to resolve the light of the companion from that of the star. This is challenging due to the extreme difference in brightness between the star and the planet and the small angular separation. Young massive self-luminous exoplanets and brown dwarfs have flux ratios in the near-infrared of $\sim 10^{-5}$. e.g. HR 8799 b,c,d,e (Marois et al., 2008, 2010). For a solar-system analogue at 10 parsec observed at visible wavelengths, looking at the stellar light reflected of the planet, an Earth-twin has a separation of 100 mas and a flux ratio of $\sim 10^{-10}$ (Traub & Oppenheimer, 2010). The flux ratio of the planet flux and the stellar flux is also called the *contrast* ratio, and direct imaging is therefore also called "high-contrast imaging". Moreover, while the planet and the star are physically separated, the properties of the imaging system (telescope) determine if the objects can be separated in the image. Imaging a point sources results in a finite size point-spread function (PSF) due to the diffraction of light. The resolving power of a telescope, the smallest angular separation it can resolve, is given by the Rayleigh criterion which equals $1.22\lambda/D$ for a circular aperture, with λ is the wavelength and

D is the diameter of the telescope. The Rayleigh criterion drives the need for ever larger telescopes or going to shorter wavelengths, resolving objects closer to the star or for looking at the same angular separation at larger distances. Being able to observing targets further from Earth increases the sample size and the additional area of the telescope helps dealing with the decreased flux. However, increasing the telescope diameter is only a partial solution for the extreme brightness ratio between the planet and star as the diffraction structure of the PSF is bright and extensive. For a telescope with a clear circular aperture, the diffraction structure has a flux $> 10^{-2}$ compared to the PSF core at the first Airy ring ($1.64\lambda/D$), and is $< 10^{-4}$ beyond $\sim 7\lambda/D$. A complicating factor is that aberrated optical systems have even more stellar flux present in these structures outside the PSF core. Ground-based telescopes look through Earth's atmosphere which creates large rapidly-changing aberrations, and therefore subtracting a reference PSFs does not work. Also, photon noise of the stellar PSF is much larger than the planet signal even if the system is diffraction limited. So, to directly image exoplanets at small separations the stellar flux needs to be suppressed by many orders of magnitude.

1.2.2 A modular view of high-contrast imaging

Directly imaging exoplanets requires instruments that have the capability to 1) correct for aberrations, 2) remove the diffraction structure at the location of the planet, 3) image the light of the planet in a way that can be used to enhance the contrast as well as enable characterization, e.g. imaging, spectroscopy, or polarimetry, 4) have a data processing infrastructure that allows for additional contrast enhancement and characterization. Such an instrument is called a high-contrast imaging system, and a general schematic of such a system is presented in Fig. 1.2. We note that contrast-enhancing techniques and characterization are closely related, but they are separate things. For example, techniques that use the spectral difference between a star and a planet enhance the contrast for a specific spectral feature, and the presence or absence of this feature within the enhanced detection limit characterizes the atmosphere of the planet. In this section we will focus on the contrast-enhancing techniques and we will shortly go over the challenges and current status of each component, although ultimately the components should not be viewed as separate.

Adaptive optics

The main problem for ground-based telescopes is Earth's atmosphere distorting the light from stars and planets. Atmospheric layers have temperature differences and potentially pressure differences that change the local refractive index of the air, and the difference in wind speed and direction generates turbulence between these layers. Turbulence in the atmosphere changes the optical path and thus arrival times of light differently for every location in the telescope pupil, distorting the wavefront temporally, and spatially and creating a PSF that is smeared-out

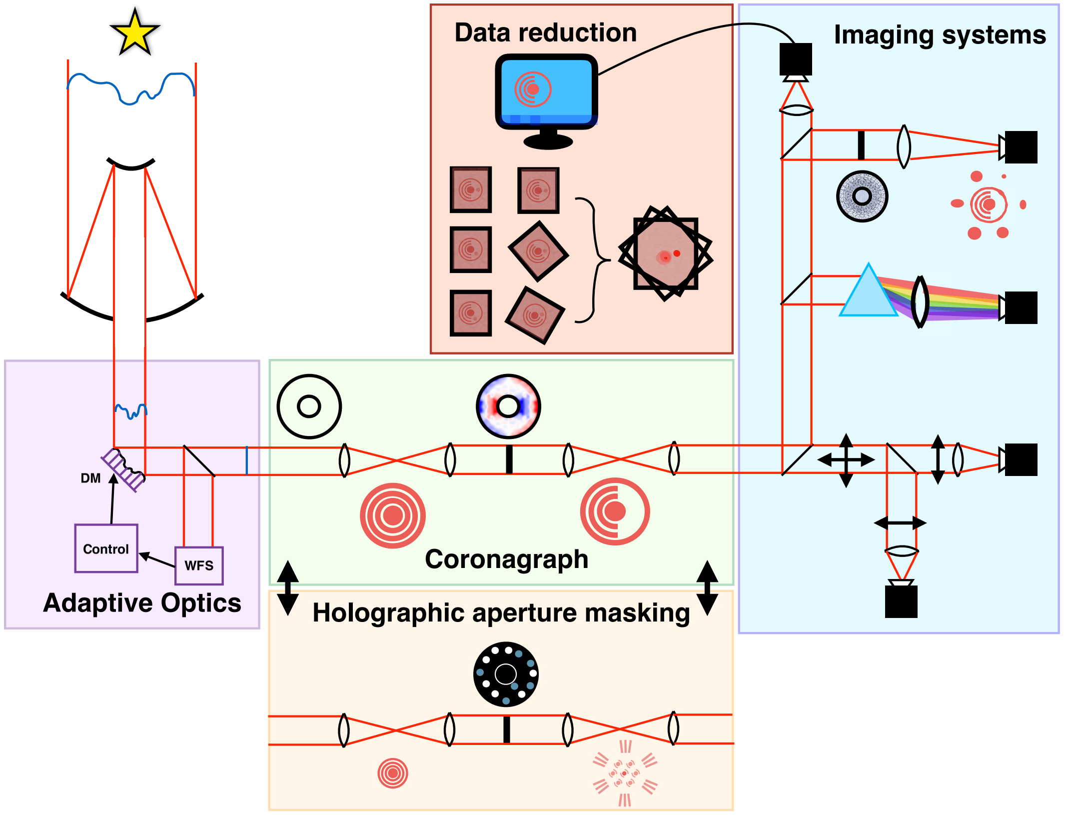

Figure 1.2: Schematic of an HCI system with five modules that combined enable the direct imaging of exoplanets. The modules are adaptive optics, coronagraph, (holographic) aperture mask, imaging system and data reduction.

compared to the diffraction limit. The turbulence is characterized by the Fried parameter r_0 (Fried, 1966), which is the coherence length of the turbulence and is ~ 10 cm for a wavelength of 500 nm and average seeing. We note that r_0 scales with wavelength as $r_0 \propto \lambda^{\frac{6}{5}}$ such that observations at longer wavelengths are less affected by turbulence. For uncorrected turbulence, the average PSF size is directly related to r_0 as the averaged angular extent is given by λ/r_0. Therefore, any increase in the telescope size beyond the r_0 is only effective in terms of spatial resolution if the atmospheric turbulence is corrected. With adaptive optics (AO) it is possible to partially correct for the turbulence and return to the diffraction limit with the current 8-m class telescopes (Fusco et al., 2016). The principle of AO is to actively measure the shape of the wavefront and correct it. A wavefront sensor (WFS) measures the wavefront by modifying the light in a way that the wavefront shape becomes an intensity modulation that can be measured with a camera. measurable quantity on a camera, like spot shifts (Shack-Hartmann WFS) or intensity variations (pyramid WFS). The Shack-Hartmann WFS (Hartmann, 1900; Shack, 1971) uses a microlens array in the pupil to create spots that shift with local wavefront tilts, directly measuring the wavefront slope. A pyramid wavefront sensor (Ragazzoni, 1996) has a pyramidal-shaped prism in the image plane to create four pupil images with intensity variations that correlate with the wavefront slope. One important property of a WFS is its efficiency, i.e. how many photons need to be captured to provide an accurate measurement of the wavefront. An efficient wavefront sensor can be operated faster or have the same performance on fainter targets. The signal of a WFS is then converted by control algorithm to shape a deformable mirror (DM), which takes the inverted shape of the wavefront with half the amplitude and thereby flattening it. A flattened wavefront restores the PSF, making it resemble the theoretical unaberrated PSF for the optical system. We note that if the DM correction is never perfect and a flattened wavefront does not necessarily result in the best contrast (Radhakrishnan et al., 2018).

When the DM is placed in the optical path before the wavefront sensor, the system forms a closed loop and the wavefront can be kept stable. A measure for the correction quality of the AO system is the Strehl ratio, which is defined as peak intensity of the corrected PSF and the perfect theoretical PSF. Even for extreme AO systems, with DMs that have many actuators controlling the mirror surface, efficient wavefront sensors and fast loop speeds (>1 kHz), the Strehl ratio is not 1. In this case, the PSF will exhibit modulations of the intensity with a size of λ/D that mimic planet signals called speckles. Speckles are coherent with the diffraction structure and are generated by many effects, but currently there are two main causes that prevent a perfect correction for a PSF at the science focal plane. First, the wavefront sensor does not measure the aberrations from optical elements between the WFS and the science focal plane. These aberrations, called non-common path aberrations (NCPA) arise from chromaticity of optics, alignment errors or surface errors, and are slowly changing due to changing gravity vectors, humidity, and temperature. Speckles generated from these aberrations are changing on timescales from minutes to hours and therefore are difficult to distinguish from planet signals (Martinez et al., 2013). Measuring NCPA is difficult as the location where you would ideally measure them is occupied by the coronagraph. Many solutions exist and most of them are summarized in Jovanovic et al. (2018). They can be separated in three categories, having a separate wavefront sensor temporarily replacing the coronagraph, using light reflected from a coronagraphic mask, or applying some known diversity to obtain the wavefront information directly from the science focal plane. In practice, all NCPA wavefront sensing techniques only gain a factor of 2-5 when tested on-sky for ground-based telescopes (Vigan et al., 2018a; Bos et al., 2019; Galicher et al., 2019). The second limiting effect for optimal AO correction is the servo-lag error, created by the finite time it takes to update the shape of the DM. Turbulence is not static as the atmosphere moves with a wind speed V_{wind} and the typical time scale for the evolving atmosphere is therefore given by $\tau_0 \propto \frac{r_0}{V_{wind}}$ (Greenwood, 1977). With wind speeds up to tens of meters per second with multiple directions in the atmospheric column a telescope looks through, the loop speeds need to be significantly higher than 1 kHz. When the loop speed is lower, the residual errors at high temporal frequency create a halo of light in the wind speed direction, the wind-driven halo (Cantalloube et al., 2018, 2020). Upgrading the loop speed is an extreme technological challenge. Another solution is to change the control loop to predict the wavefront by extrapolating the wind speed and the previous evolution (Hardy, 1998; van Kooten et al., 2019). Without predictive control the AO is fundamentally limited by photon noise at the 10^{-4}-10^{-6} level (Guyon, 2005; Males & Guyon, 2018).

For space-based high-contrast imaging systems the performance is also limited by wavefront control, albeit at a very different contrast level. The thermal load variation caused by solar radiation results in slow drifts in the wavefront and vibration from the reaction wheels result in high-frequency wavefront aberrations (Shi et al., 2017). Also, it is possible that the deformable mirror itself can drift (Seo et al., 2019). Low-order coronagraphic wavefront sensors are used in combination with focal-plane wavefront-sensing techniques to achieve the 10 picometer RMS wavefront that is required for 10^{-10} contrast (Steeves et al., 2020). An overview of current work on wavefront sensing for space-based missions was given by Pueyo et al. (2019). Adaptive optics, including both hardware and software, is the most critical system that largely sets the contrast limit for a high-contrast imaging instrument.

The coronagraph

After correction of the wavefront, the diffraction structure close to the PSF core is still much brighter than the signal of planets. A coronagraph is an optical device that suppresses this diffraction structure. The advantage of a coronagraph is two-fold. By suppressing the diffraction structure, the photon noise of the stellar light is reduced, and second, the influence of speckles is suppressed. Therefore, a coronagraph significantly enhances the signal-to-noise ratio of the planet signal. The first coronagraph was developed by Bernard Lyot to image the solar corona by masking the disk of the sun and blocking the diffracted light in a consecutive pupil plane (Lyot, 1939). Since then, many different coronagraphs have been designed and tested as is summarized in Mawet et al. (2012) and Ruane et al. (2018). These coronagraphs can be compared in performance by looking at five properties: inner working angle, contrast, sensitivity to low-order aberrations, throughput, and chromaticity. The *inner working angle* (IWA) is defined as the smallest angular separation at which the total energy throughput of an off-axis source reaches 50% of the maximum throughput, or where the contrast reaches a threshold value (Ruane et al., 2018). The IWA is not necessarily the same as the diffraction limit, but can always be expressed as a factor of the diffraction limit set by the telescope diameter. We note that coronagraphs also have an outer working angle, which has the same definition as the IWA but for the outer edge of the dark zone. The *contrast* is defined as the flux ratio with respect to the star where a point source can significantly (5σ) be detected (Jensen-Clem et al., 2017). For a coronagraph design, the contrast is then the (spatially variant) suppression of the starlight divided by the coronagraphic throughput for a clear telescope aperture, measured in a circle with a diameter of approximately the diffraction limit. In telescopes the optical aberrations reduce the contrast but this is not the same for any coronagraph. Some coronagraphs are more resistant to low-order modes at the cost of a larger (theoretical) inner working angle, yet the measured contrast with these aberrations might be better at the smallest separations (Mawet et al., 2010). Lastly, exoplanet characterization requires multi-wavelength observations or spectroscopy. Coronagraphs that deliver good contrast over large bandwidths have an improved the observation efficiency and higher signal-to-noise per spectral bin.

These coronagraphic properties are easily visualized for a Lyot coronagraph, which has an opaque mask in the focal plane that blocks the starlight, see Fig. 1.3. Another amplitude mask (or Lyot stop) in the following pupil plane blocks the stellar light that is diffracted around the opaque focal-plane mask. The inner working angle is then determined by the focal-plane mask radius, the throughput of planets far beyond the IWA is given by the Lyot stop area compared to the actual pupil size, and the chromaticity is largely determined by the wavelength scaling of the PSF. The Lyot coronagraph is a focal-plane coronagraph, as the opaque mask that blocks the star is in the focal plane. Other focal-plane coronagraphs have different focal-plane masks, but operate on the same principle with a Lyot stop, e.g. the vector vortex coronagraph (VVC) (Mawet et al., 2005a), phase-induced amplitude apodization complex mask coronagraph (PIAACMC) (Guyon et al., 2005). If a phase mask is used in the focal plane (VVC, PIAACMC) the phase pattern results in destructive interference in the pupil. Focal-plane coronagraphs have a theoretical performance in both inner working angle and throughput is better than the other type of coronagraphs that operate in the pupil plane. Moreover, it has been shown that the use of focal-plane phase masks result in an improved performance over amplitude masks (Mawet et al., 2009a; Por, 2020) . Yet, because focal-plane coronagraphs are sensitive and have small inner working angles, they are highly sensitive to tip-tilt aberrations that can be caused by vibrations.

Pupil-plane coronagraphs have a different philosophy compared to focal-plane coronagraphs, as they do not block the starlight but rather change the shape

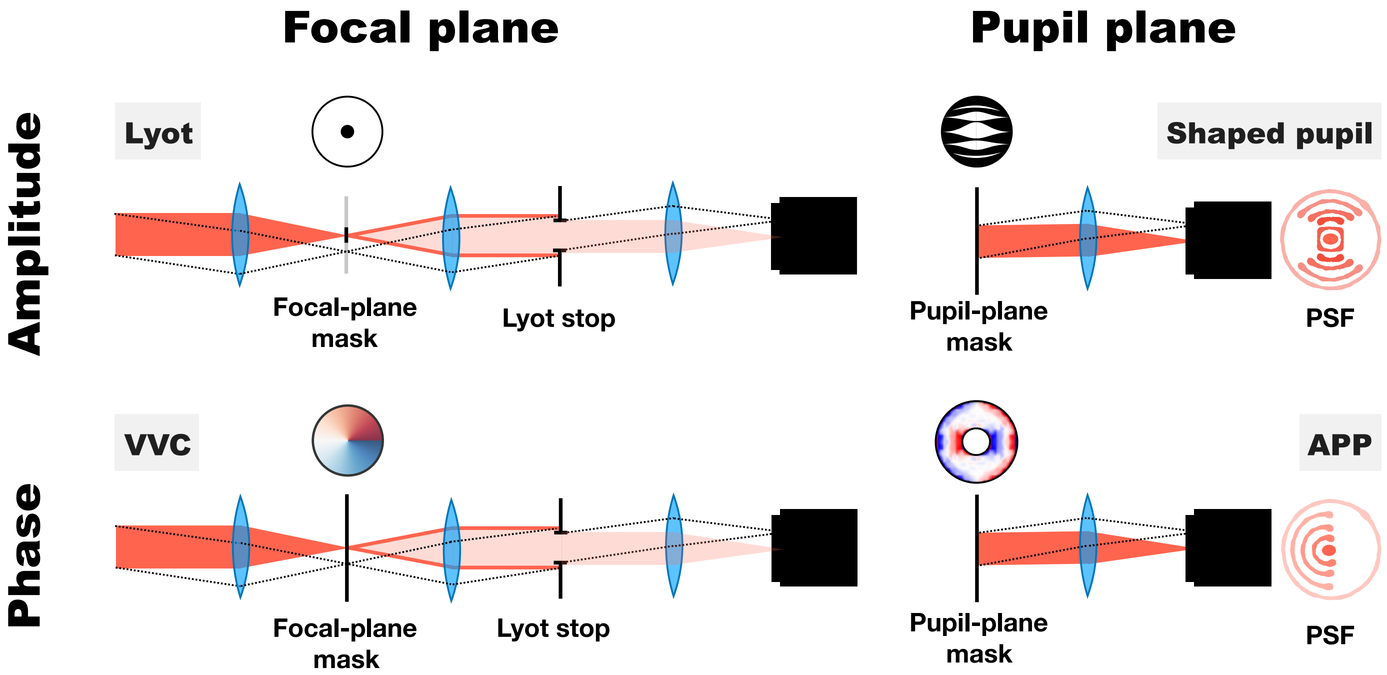

Figure 1.3: Schematic of four types of coronagraphs, having phase or amplitude masks in the focal plane or pupil plane.

of the PSF with a region where the flux is reduced. This so called dark zone is created by nulling the starlight with either a phase or amplitude mask, e.g. the apodizing phase plate (APP) (Codona et al., 2006; Kenworthy et al., 2007; Snik et al., 2012) or the shaped pupil (Kasdin et al., 2003) respectively. Both are shown in Fig. 1.3. Pupil-plane coronagraphs change the shape of all objects in the field-of-view in the same way, making the coronagraphs tip-tilt insensitive. In addition, they occupy a single pupil plane, making it easy to install them in existing high-contrast imaging systems. The advantage of phase patterns over amplitude masks is that it enables the creation of one-sided dark zones with smaller inner working angles. Moreover, it can be shown that for annular dark zones the phase-only solution always provides a better performance compared to amplitude masks (Por, 2017). A detailed description of the APP coronagraphs can be found in chapter 2. A third type of coronagraph are the hybrid coronagraphs, having a phase or amplitude mask in both the pupil plane and focal plane. With two masks the design freedom is larger, making it easier to adapt to any pupil shape (Soummer, 2004), or increase the bandwidth (Soummer et al., 2011b). For the Nancy Grace Roman Space Telescope (previously named WFIRST), two hybrid coronagraphs have been selected, the (hybrid) shaped pupil coronagraph and the hybrid Lyot coronagraph (HLC). The shaped pupil coronagraph has an amplitude pupil-plane and focal-plane mask in addition to a Lyot stop (Balasubramanian et al., 2015). The HLC uses a static offset on two deformable mirrors in combination with a standard Lyot setup (Trauger et al., 2016). A different version of the Lyot coronagraph, the apodized pupil Lyot coronagraph (APLC), is commonly used for ground-based observations (Macintosh et al., 2006; Beuzit et al., 2019). The APLC has an amplitude mask in the pupil plane with a standard Lyot setup (Soummer, 2004). Replacing the amplitude mask in the pupil plane with a phase mask, the phase apodized pupil Lyot coronagraph (PAPLC), results in an improved performance (Por, 2020), and enables one-sided dark zones.

Over the last decade, coronagraph designs have improved for arbitrary apertures both terms of contrast and inner working angle (Ruane et al., 2016; Por, 2017; N'Diaye et al., 2018; Por, 2020). Due to rapid technological advancements, the coronagraphic performance has also been demonstrated in the lab. For example, the Lyot coronagraph has delivered extreme stellar suppression ratios down to 4×10^{-10} between 3-8 λ/D for 10% bandwidth (Seo et al., 2019). These coronagraphs are soon ready to use for the next generation of space-based missions, where the aberrations are small. On the other hand, ground-based instruments are limited by the AO system to a contrast of $\sim 10^{-5}$. It can be shown that switching between coronagraphs in AO-limited systems does not result in a significantly improved performance (Carlomagno et al., 2016). The parameter space for coronagraph design has therefore shifted to chromaticity (ground- and space-based) and robustness against low-order aberrations (space-based). Comparing coronagraphs with the aforementioned metrics is relatively simple but does not consider all the differences between coronagraphs. For example, some coronagraphs are better for focal-plane wavefront sensing or less sensitive to the shape of a telescope pupil or have different dark-zone shapes. These properties also impact the operation and

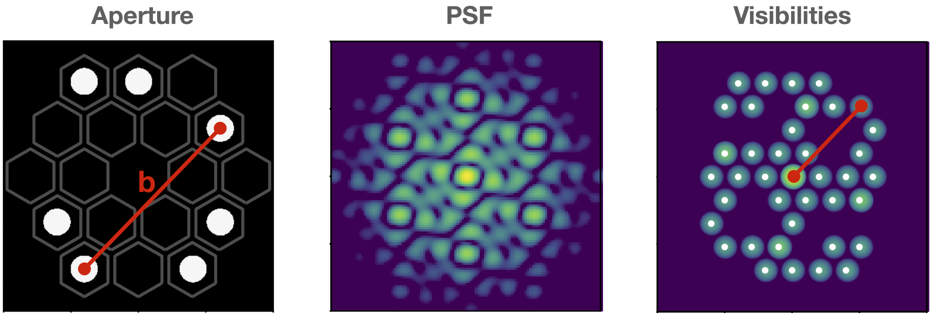

Figure 1.4: *Left:* Layout of a 7-hole aperture mask where every hole pair has a unique vector called a baseline (b). *Middle:* Simulated PSF of the aperture mask, which is the combination of all fringes generated by the 21 hole pairs. *Right:* The Fourier transform of the PSF (visibilities), decomposing the PSF in the individual frequencies corresponding to the baselines.

performance on-sky. Only in recent years, a true comparison was attempted by considering a full observing sequence that would be optimal for each coronagraph and looking at the exoplanet yield assuming a planet population (Stark et al., 2019).

Aperture masking

A technique complementary to coronagraphy in terms of detecting objects at small separations is sparse aperture masking (SAM). SAM is an interferometric technique and works by turning a telescope aperture into an interferometric array using an opaque mask with small holes in the pupil plane (Haniff et al., 1987; Tuthill et al., 2000). A commonly used version of SAM uses a mask with holes that are placed in a non-redundant fashion, which means that each baseline (the vector that connects two apertures) appears only once. The PSF of such a mask is an interferogram which contains many fringes with unique spatial frequencies corresponding to these baselines. By recovering the phase and amplitude of all fringes in the interferogram, it is possible to reconstruct an image of the observed object. The fringe phase and amplitude recovery is usually done by directly fitting all fringes in the interferogram at the same time (Lacour et al., 2011a; Greenbaum et al., 2014) or by Fourier transforming the image to create the visibility plane (Tuthill et al., 1999; Sallum & Eisner, 2017). The conversion to an image is done using the CLEAN algorithm (Högbom, 1974) or maximum entropy method (Gull & Skilling, 1984; Sivia, 1987). SAM has two distinct advantages over direct imaging. First, the fringes of the PSF have a first null at $0.5\lambda/B$ instead of $1.22\lambda/D$, where B is the longest baseline, resulting in a reduction of the full width at half maximum of the PSF by a factor ≈ 2. The diffraction limit of SAM is therefore

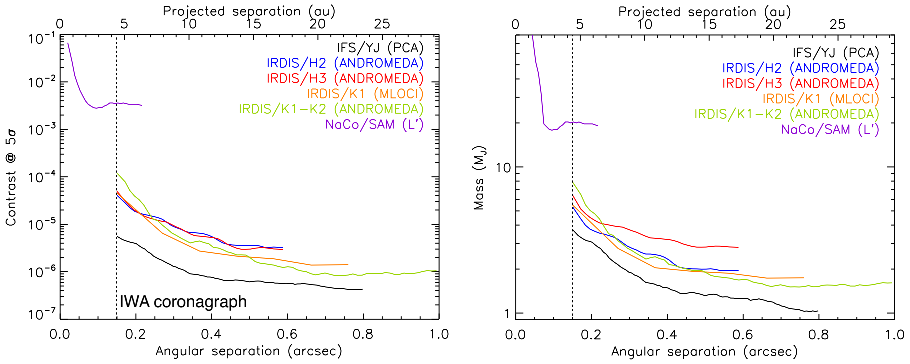

Figure 1.5: *Left:* 5σ-contrast of observations of 51 Eridani using NACO/SAM (L'), SPHERE/IRDIS, and SPHERE/IFS. *Right:* Same as left, but converted to mass using models from (Baraffe et al., 2003, 2015) and BT-Settl models (Allard, 2013). Adapted from (Samland, M. et al., 2017).

twice as small for the same telescope for a baseline that spans across the pupil. Second, the non-redundancy can be exploited to reject the effect of atmospheric or instrumental aberrations on the fringe phases and amplitudes. In particular, there are robust observables called closure phases that are independent of these aberrations but depend on the source structure. Closure phases are formed by taking the sum of phases around baselines forming a closed triangle of subapertures in the pupil. It was this combination of properties of SAM that allowed for imaging the regions closest to stars before adaptive optics became a standard practice in astronomy (Tuthill et al., 1999).

The downside of sparse aperture masks, such as those in VLT/SPHERE (Lacour et al., 2011b) and Keck/NIRC2 (Tuthill et al., 2006), is that they block $80 - 90\%$ of the incident light. Moreover, the closure phases are only stable against static phase aberrations and fast imaging is required to combat the influence of turbulence. Thus, sparse aperture masking was limited to bright targets, however with the invention of AO the requirement on the imaging speed could significantly be relaxed. When SAM is used in concert with AO, SAM provides extremely stable closure phases that resulted in a leap in sensitivity and contrast (Tuthill et al., 2006). The superior calibration particularly of closure phases makes SAM more sensitive than coronagraphs, probing separations that are otherwise dominated by aberrations ($< 1 - 2\lambda/D$), e.g. Gauchet et al. (2016); Cheetham et al. (2016); Samland, M. et al. (2017). The parameter space for exoplanet detection is also shown in Fig. 1.5. Most recent results show that SAM at VLT/SPHERE can reach a 5σ contrast of $\sim 10^{-3}$ down to 30 mas (0.6 λ/D in K-band) (Claudi et al., 2019; Pérez et al., 2020).

Imaging systems and data reduction

The imaging system is closely connected to the data reduction process and together they also represent additional methods of enhancing the contrast. Moreover, what information can be recovered from the planet signal is directly determined by the imaging system. We reiterate that contrast-enhancing techniques and characterization, e.g. through spectroscopy and polarimetry, are separate things. The physical differences between the star and planet generate differences in the stellar flux or planetary flux that can be exploited to enhance the contrast. There are four methods that we will briefly discuss: reference star differential imaging (RDI), angular differential imaging (ADI), spectral differential imaging (SDI), and polarimatric differential imaging (PDI). The first two methods use the fact that the planet is spatially separated from the star.
ADI: Angular differential imaging is currently the most widely used differential technique. The technique makes use of the sky rotation with respect to the telescope pupil for an alt-azimuth telescope (Marois et al., 2006a). If the pupil is stabilized the sky rotates with respect to the PSF structures, e.g. from spiders or speckles, and the PSF structures remain in a mean image of all the data. However, off-axis objects rotate with the parallactic angle and the mean will average this to a smeared and reduced signal. Subtracting the mean image from every frame therefore removes the unwanted PSF structures and derotating and stacking the residuals leads to a great enhancement of the detection limit. More advanced methods of combining the images to create a better reference PSF produce better results (Lafreniere et al., 2007). Another method creates subtracts the principal components from the data before derotation, i.e. principal component analysis (PCA) (Soummer et al., 2012). ADI works best for larger separations, where the size of the diffraction structures is much smaller than the rotation path of the object. It takes much longer for an object at small separation to have rotated by a diffraction width than at larger separations. If the rotation is smaller than the object size then the object is partially subtracted from itself, i.e. self-subtraction. Self-subtraction can also happen for more face-on circumstellar disks, such that ADI can distort the retrieved disk shape (Sissa et al., 2018; Ruane et al., 2019).
RDI: With RDI an image of a reference star is subtracted from the data to remove the stellar PSF or the target, and was already used by Smith & Terrile (1984) to reveal the circumstellar disk around β Pictoris. RDI assumes that the reference star does not have companions and that the reference PSF is a good representation of the target PSF. Space-based observations have an extremely stable PSF, and by using a library of PSFs that are aberrated differently gathered over many observations it is possible to even remove the full non-coronagraphic diffraction structure. This was demonstrated by Soummer et al. (2011a), who detected HR 8799 b,c,d in data of the Hubble Space Telescope by using RDI to gain approximately two orders of magnitude in contrast. Interestingly, it was archival data of 1998, taken a decade before the first detection of HR8799 by Marois et al. (2008). Examples like this show the true power of data reduction and how far this field has progressed in the last decade and a half. RDI also works for ground-based

observations, where a stable AO performance minimizes the changes between the PSF of a reference star and the target. Observing with a 1.5-m subaperture on the Hale Telescope, Serabyn et al. (2010) were able to detect HR 8799 b,c,d using RDI, with HR8799 d at only twice the diffraction limit (Serabyn et al., 2010). RDI can have an improved performance up to a factor of 5 compared to ADI at the smallest separations (Ruane et al., 2019). In addition, it is less prone to self-subtraction which makes it also useful for circumstellar disks. A different implementation of RDI is possible with the vAPP coronagraph, which creates two copies of the coronagraphic PSF. One can be used as reference for the other PSF by rotating it 180 degrees (Otten et al., 2017).

SDI: Spectral differential imaging encompasses different methods that use simultaneous multi-wavelength observations to differentiate stellar diffraction structures from the planet PSF (Sparks & Ford, 2002). These simultaneous multi-wavelength observations are obtained with an integral field spectrographs (IFS), which combines imaging with spectroscopy. The classical version uses the similarity of the stellar PSF between the IFS observations to create a reference PSF. The reference PSF at a separated wavelength bin will have a different scale due to wavelength scaling. As the separation of the planet and the star is not wavelength dependent, scaling the reference PSF will move the planet in the scaled image. Similar to ADI, taking a mean of these scaled images gives a good PSF model while the planet signal is suppressed. Subtracting the scaled PSF model from the unscaled images for each wavelength reveals the planet. However, in essence this does not use the spectral information that the star has a different temperature and constituents than the planet. This is difficult with the current integral field spectrographs as they have a spectral resolution ($\lambda/(\Delta\lambda)$) between 20-100, e.g. SPHERE/IFS (Claudi et al., 2008), GPI/IFS (Chilcote et al., 2012), SCExAO/CHARIS (Groff et al., 2014), LBT/ALES (Skemer et al., 2018). A downside of SDI is that large spectral bandwidths are required to minimize self-subtraction close to the star. For example, observations of a single band ($\Delta\lambda/\lambda \sim 20\%$) have self-subtraction within $\sim 6\lambda/D$, which also influences the retrieved spectrum. Therefore, IFS data with low-resolution spectrographs is usually treated as completely separate for each wavelength bin.

Medium- and high-resolution IFSs offer a larger tool box due to resolving spectral lines of the stellar and planetary atmosphere. These new tools could be considered a branch of spectral differential imaging as they do use the spectral differences to reject stellar light. A first tool is cross-correlation with a molecular template (Snellen et al., 2010). After removing an averaged and scaled spectrum of a star from each pixel, their residual spectrum should be mostly free of stellar contamination. If a planet is present, the residual spectrum contains a low-signal to noise spectrum of the planet with many molecular features that are too faint to detect. Cross-correlation with a molecular template boosts the signal-to-noise by combining the signal of all molecules into a single signal, and this has been used to detect a few different molecular species in atmospheres of gas giants (Snellen et al., 2015; dit de la Roche et al., 2018; Hoeijmakers et al., 2018a). High-resolution spectrographs with a resolution of $\sim$ 100.000 can resolve the spectral shift (or Doppler

shift) from the movement of the planet around the star. Cross-correlation is again used to boost the signal and the radial velocity of the planet can be determined, which characterizes the orbit and mass of the planet (Snellen et al., 2014).
PDI: The fourth method of polarization differential imaging uses differences in polarization state of the light of the star and surrounding objects. Polarization refers to the preferred oscillation direction of a group of electromagnetic waves in a beam of light. If there is no preferred oscillation direction, the beam is called unpolarized. A beam can be composed of the combination of polarized and unpolarized light, and the degree of polarization is given by the fraction of polarized over unpolarized light. PDI uses that stellar light is highly unpolarized, while scattered light is linearly polarized. Circumstellar disks present large scattering surfaces and PDI has been widely used to discover them (de Boer, J. et al., 2016; Avenhaus et al., 2018). Exoplanets scatter stellar light resulting in a significant degree of polarization, and thus PDI could be used to enhance the contrast. Moreover, it is expected that young gas giants also emit partially polarized light in the thermal infrared, yet the degree of polarization is low ($< 1\%$) (Stolker, T. et al., 2017). Instrumental polarization, i.e. changes in polarization state due to (retarding) optics in the instrument, can result in incorrect measurements of the polarization. However, recent work on instrumental polarization in VLT/SPHERE showed that it can be calibrated using a Mueller matrix model to an absolute polarimetric accuracy of $< 0.1\%$ (De Boer et al., 2020; Van Holstein et al., 2020). Current issues with PDI are polarization aberrations and beam-shifts [4]. The true potential of PDI was shown by van Holstein et al. (2017) by reaching a 1σ contrast of 2×10^{-7} on HR 8799. This resulted in a non-detection, giving an upper limit on the degree of polarization of the HR 8799 planets $< 1\%$ (1σ).
The aforementioned differential techniques improve the contrast, however, this is not the full picture[5]. As discussed in section 1.1, spectroscopy enables the characterization of the atmospheres of exoplanets by measuring its constituents and bolometric flux. Polarimetry can reveal asymmetric structures like oblateness and patchiness clouds for gas giants (De Kok et al., 2011; Stolker, T. et al., 2017; van Holstein et al., 2017) and even determine the presence of liquid oceans (Stam, D. M., 2008; Klindžić et al., 2020) or even life (Patty et al., 2019). Temporal variations can reveal existence of patchy clouds and even more if combined with the other techniques (Apai et al., 2013).

To summarize, detecting and characterizing exoplanets with direct imaging is extremely challenging and requires a large-aperture telescope, high-precision wavefront sensing and correction, a coronagraph with a small inner working angle to suppress the stellar diffraction halo by masking or diffracting stellar light, advanced observational and data-reduction strategies and intricate optical measurement systems, such as polarimetry or integral field spectroscopy (Ruane et al., 2018; Jovanovic et al., 2018; Snik et al., 2018).

---

[4] van Holstein in prep.

[5] pun intended

1.3 Ground-based and space-based high-contrast imaging

The high-contrast imaging instrument layout is applicable both to ground-based and space-based high-contrast imaging. It is the atmosphere that makes that these systems operate in entirely different regimes in terms of contrast. However, we will show here that despite the atmosphere, they are *complementary* to each other.

1.3.1 The compatibility of ground and space

As explained in section 1.2.2 and 1.2.2, the turbulence in the atmosphere degrades the contrast levels that can be reached compared to lab results by orders of magnitude. While the impact of turbulence decreases for longer wavelengths, the thermal background from the atmosphere becomes the limiting factor beyond ~ 3.0 μm (L-band). Earth's atmosphere also has significant molecular absorption features resulting in an incomplete coverage of the full electromagnetic spectrum. We note that these molecules are also likely to be present in exoplanets similar to Earth and any other type of planets, e.g. super-Earths, mini-Neptunes and gas giants. Examples of these molecules are H_2O and CO_2 and detecting these molecules is critical for our understanding of their atmospheres. With space observatories the aforementioned atmospheric effects are no longer an issue and a full wavelength coverage can be achieved. Therefore, it seems that space-based observatories have a clear advantage over ground-based telescopes. Yet, this advantage was not yet fully exploited due to technology only having been matured over the last decade. No existing or decommissioned space-based observatory has had a dedicated high-contrast imaging mode with adaptive optics. Only lab demonstrations have reached the performance that would be good enough to image planets in reflected light, i.e. 10^{-10} (Traub & Oppenheimer, 2010; Seo et al., 2019). Moreover, it will take over a decade to launch a big space mission that works with the current technology. This time is used to create robust systems that do not need servicing or repairs, which is impossible for space missions that have orbits around the second Lagrangian point. It also means that the current technology is likely not launched until 15 years from now. Lastly, space-based systems are on average an order of magnitude more expensive and need to fit onto a rocket. A most important consequence is that the diameter of the primary mirror can not be very large compared their ground-based counterparts, limiting the spatial resolving power. By comparison, the next generation space telescope, the James Webb Space Telescope, will have a primary mirror diameter of 6.5 m, while the next generation ground-based telescope, the Extremely Large Telescope, will have a diameter of 39 meters. Besides mirror diameter, another advantage of ground-based systems is that they are great for rapidly prototyping technology and software. The difference in resolving power and contrast limit between ground-based and space-based systems is the crux of the harmony between the two, as is shown in Fig. 1.6. Both types probe a different parameter space and provide a comple-

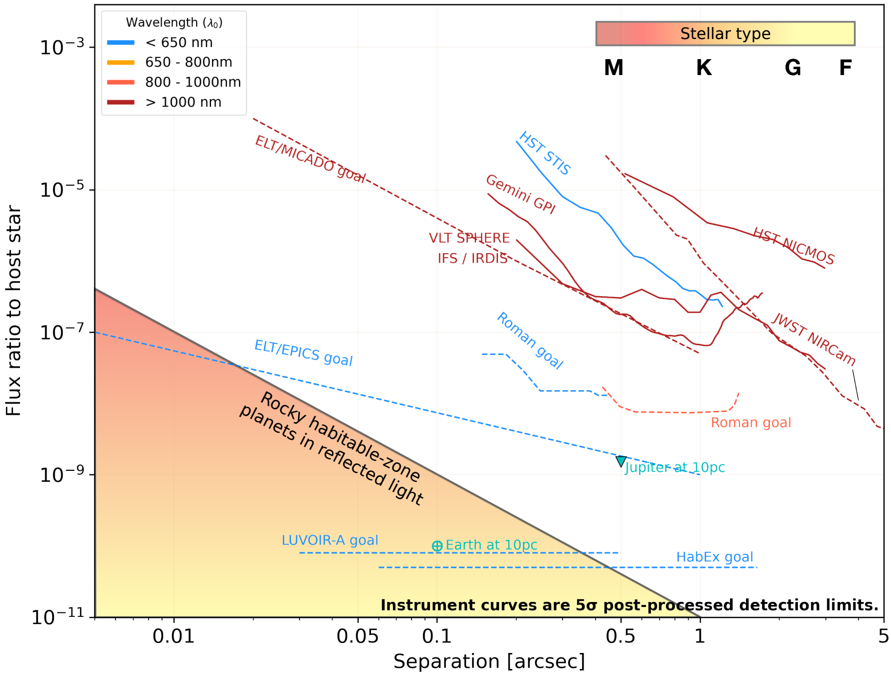

Figure 1.6: Measured or predicted contrast curves of current and future high-contrast imaging facilities. Created using `https://github.com/nasavbailey/DI-flux-ratio-plot`.

mentary look on the exoplanet population, as is most clear for the future space- and ground-based missions. Future large ground-based telescopes are able to look closer-in at a moderate contrast, which is ideal for looking for exoplanets in the habitable zone around M-dwarfs. On the other hand, space-based observatories are stable enough to reach extreme contrasts further out, which is necessary for observing the habitable zone around solar-type stars. Moreover, current telescopes are already oversubscribed and with the next generation this will be worse. It is unlikely that a significant fraction observing time can be spent on large exoplanet surveys, so next-generation telescopes are likely to spend the time characterizing exoplanets found by indirect measurements. These numbers will be large due to the fast amount of current and future missions and surveys with indirect detection methods that are underway and planned, e.g. *Gaia*, TESS, JWST, HARPS3 and ESPRESSO (Snellen et al., 2019). Following up on these targets can and should be divided between all available telescopes to maximize the scientific output and understanding of the planet population. A more in-depth analysis of the timeline and impact of these future missions can be found in section 1.6. Lastly, space-based and ground-based telescopes have similar architectures and the development of subsystems is intertwined. With space operations requiring technology to have reached the maximum technology readiness level, many systems have been further developed from a ground-based system. This is highlighted in balloon missions like HiCIBaS (Marchis et al., 2018) and PICTURE-C (Mendillo et al., 2019), providing a platform to test technology in a space-like environment.

1.3.2 The current state and limitations

With the absence of space-based high-contrast imagers, the scientific output of high-contrast imaging during the last decade has been dominated by ground-based facilities. Mostly driven by technological advances of hardware and new methods of data reduction, the field has transitioned from photometric detection at large separations to characterization of planets a few times the diffraction limit (Rajan et al., 2017; Lagrange et al., 2019). This has been accompanied with the creation of many high-contrast imaging systems at manyx‘ 8-m class telescopes around the world, spanning all astronomical observing bands between 500 nm and 10 μm. Especially the use of an integral field spectrograph enabled the spectral characterization of brown dwarf and exoplanet companions, and polarimetry has been widely used to detect and characterize circumstellar disks. We note that the impact of the development of ever more advanced models of exoplanet atmospheres should not be forgotten in the understanding of observational data. While the improvements lead to a great leap in knowledge of stellar surroundings, the amount of directly detected exoplanets has been low (< 10). The absence of detected exoplanets did put constraints on the demographics of young giant exoplanets by looking at the fraction of stars that have significant detections (Vigan et al., 2020; Nielsen et al., 2019). Two extensive surveys, SHINE and GPIES with SPHERE and GPI respectively, have been completed and observed for hundreds of hours and hundreds of stars. Their results are shown in Fig. 1.7. These surveys clearly demonstrated

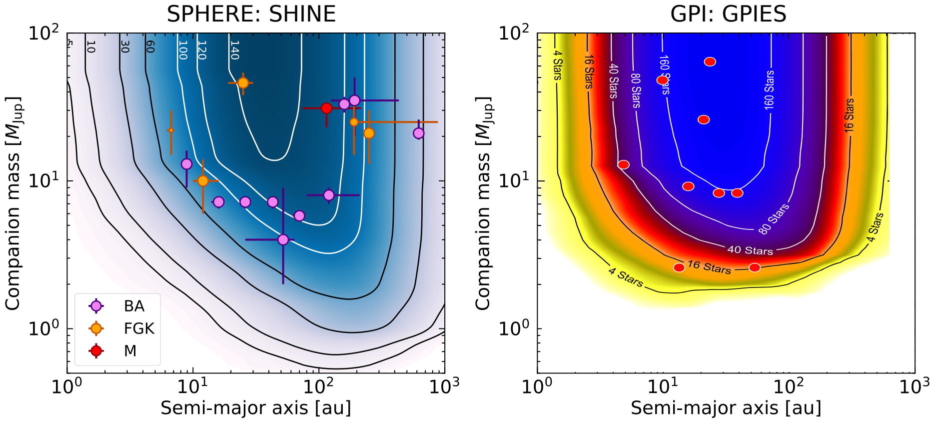

Figure 1.7: *Left*: Depth of search of the SHINE survey for the 150 stars in the sample, from Vigan et al. (2020). *Right*: Depth of search for the first 300 stars observed by GPIES, from Nielsen et al. (2019). The contour lines give the numbers of stars around which the survey is sensitive to substellar companions as a function of mass and semimajor axis. The circles represent the detected substellar companions in the sample.

that the current systems lack the sensitivity and the angular resolution to detect a significant fraction of the exoplanet population. Planned upgrades aim for higher contrasts closer at the closest separations (Chilcote et al., 2018; Boccaletti et al., 2020). Interestingly, some of these limits can be pushed by instruments not necessarily designed for high-contrast imaging. Examples are the detection of PDS 70 c with MUSE, an AO-assisted, non-coronagraphic IFS (Haffert et al., 2019) and the direct detection β Pictoris c with GRAVITY (Nowak, M. et al., 2020). The focus of high-contrast imaging has therefore shifted to developing improved systems, both by decreasing the inner working angle and increasing the contrast performance. A large focus is on the AO-system as this is the limiting factor for all systems, making them more sensitive, faster and adding predictive control. Non-common path aberrations are the next limiting factor, and many systems that apply focal-plane wavefront sensing or low-order wavefront sensing are being investigated (Jovanovic et al., 2018). Some of these solutions are integrated with the coronagraph, e.g. cWFS (Wilby et al., 2017) or SCC (Galicher et al., 2010), and show an integrated way of looking at the high-contrast imaging system. We note that post-processing techniques like ADI can also be seen as integration between the observing strategy and data reduction. However, recently there has been a large increase in new concepts that are being investigated. For example, a coronagraph design that is optimized for the injection of light in a single-mode fiber for high-resolution spectroscopy (Ruane et al., 2018; Por & Haffert, 2020; Haffert et al., 2020). Other examples include combining spectroscopy with polarimetry in Subaru/SCExAO

(Lozi et al., 2019), adapting the coronagraph or dark zone control real time depending on the atmospheric conditions (Carlotti et al., 2018; Radhakrishnan et al., 2018), the integration of photonics with interferometry to decrease the instrument size and increase stability (Jovanovic et al., 2016), or the creation of low-noise detectors with spectral resolving powers like MKIDs (Baselmans, 2012; Meeker et al., 2018). Many of these examples are focused at improving the characterization of exoplanets, which is the ultimate goal of high-contrast imaging, and their timing is fortunate. There will be room for testing these developments on current generation telescopes once the ELTs come online, and the lessons-learned can be implemented in the second-generation ELT instruments to fully exploit the large diameters.

1.4 Broadband enabling technologies

With spectroscopic characterization of exoplanets becoming the main focus of high-contrast imaging, each subsystem of the instrument needs to facilitate broadband technology. For ground-based systems the AO-system delivers good correction over large bandwidths and is common path with multiple imaging systems observing at bands spanning more than an octave in wavelength. Instruments like VLT/SPHERE (Beuzit et al., 2019) and Subaru/SCExAO (Lozi et al., 2018) even have a common coronagraph for these imaging systems. However, most coronagraphs have an optimal performance in a single band ($\Delta\lambda/\lambda \sim 20\%$) due to chromaticity of the phase (PIAACMC, Martinez et al. (2020)) or chromaticity of retardance (VVC, **?**), or the PSF scaling on the focal-plane mask (Lyot). Observing in a single band decreases the observing efficiency and flexibility. Capitalizing on the availability of all instruments is enabled by broadband coronagraphs. The broadband performance of space-based systems is inherently limited by the chromaticity of the wavefront control, reducing the possible instantaneous bandwidth to 20%. To facilitate characterization, the space-based systems are capable of observing over a much wider bandwidth, resulting in the use of many different coronagraphs (HabEx Study Team, 2019). All these coronagraphs require a different calibration due to manufacturing errors. A single broadband coronagraph would make the calibration easier and create flexibility in the observing modes and increases the efficiency of spectroscopy. So, a high-performance broadband coronagraph is a necessity.

Both for some focal-plane coronagraphs and pupil-plane coronagraphs it has been shown that solutions with phase masks instead of amplitude masks provide the most optimal combination of inner working angle and throughput, (Mawet et al., 2009a; Por, 2017, 2020). Here, we will discuss how to make complex phase patterns and how to make them achromatic.

There are different techniques to generate phase patterns. The most common technique generates differences in the local optical path length to offset the phase (Born & Wolf, 2013). Optical path differences (OPD) are created by travel time variations of light, either by changing the travel distance d, or the speed through the differences in refractive index n. A phase shift caused by the OPD is also called the dynamic or classical phase shift, and is given by

$$\phi = \frac{2\pi}{\lambda} nd. \tag{1.1}$$

Changing either n, d, or both results in a phase shift and many different technical implementations exist. For example, a deformable mirror changes only d. Moreover, thickness variations Δx of materials with a high refractive index n_{plate} compared to the refractive index of the embedded medium n_{air} to create a phase delay $\Delta\phi$, given by

$$\Delta\phi = \frac{2\pi(n_{\text{plate}} - n_{\text{air}})\Delta x}{\lambda}. \tag{1.2}$$

This technique of phase generation is well known and has many applications, e.g. lenses. Another technique uses changes in refractive index of an optic axis of a liquid-crystal birefringent medium (= retarder) to introduce phase differences. These changes in refractive index are created by applying a voltage to the liquid crystals, modifying their orientation along the axis of propagation of the incoming light. By creating a device with different pixels, each with their own voltage regulator, any phase pattern can be created within the limits of the refractive index modulation. Such a device is called a spatial light modulator (SLM) (Love, 1997). All these implementations of dynamical phase have their own advantages, but they also have two common downsides. The generated phase is wavelength-dependent and deviating from the optimal relative phase degrades the performance of the coronagraph. Moreover, it is difficult to accurately create freeform phase patterns for these transmissive optics, limiting the parameter space for coronagraphs like the APP (Codona et al., 2006). An SLM is an exception to this last point, however it suffers from polarization effects (Yeh, 2007).

Ideally, the phase plates of coronagraphs would be built as a device that is capable of generating arbitrary achromatic phase differences. Such a device can be realized through geometric phase, which was discovered by S. Pancharatnam in 1956 (Pancharatnam, 1956), and later rediscovered for quantum mechanics by M. Berry in 1984 (Berry, 1984). Geometric phase, now also called Pancharatnam-Berry phase, arises when light travels through a retarder with a locally changing *orientation* of the fast-axis rather than a changing thickness or refractive index (Escuti et al., 2016). First, we will go into the properties of the geometric phase, then we will present a short derivation using Jones matrices, followed by an intuitive explanation of geometric phase that is connected to the history of geometric phase, and we conclude with the technical implementation of geometric-phase optics using liquid-crystal technology.

1.4.1 Properties of the geometric phase

Geometric phase, as the name implies, only depends on the local geometry of the optic it travels through. For an optic made out of glass, the refractive index is the same for any orientation of the light (or linear polarization state), and geometric phase is not generated. On the other hand, birefringent materials are anisotropic, meaning that the refractive index changes depending on the polarization state of the incoming light. Therefore, their orientation with respect to the polarization state of light matters and different orientations lead to changes in polarization state and phase of the light that passes through the optic (Pancharatnam, 1956; Escuti et al., 2016). This orientation is defined as an angle between the oscillation direction of a ray of light and some axis of anisotropy in the birefringent material, i.e. the crystal axis. Optics from birefringent materials (= retarder) are commonly manufactured with the anisotropy in a single direction, i.e. the optic axis, that is parallel to the front surface of the optic. The refractive index is n_o for linearly polarized light that oscillates parallel to this optic axis, while the refractive index for the orthogonal polarization state is n_e. Either of the two axes with the lowest refractive index is called the fast axis, and the axis with the highest refractive index is called the slow axis. The (dynamic) phase delay between these two axes is the retardance and depends on the thickness and refractive indices of the optic, and the wavelength of the light. If the linear polarization state does not align with any of the two axes, the light-wave can be decomposed in two components that are parallel and orthogonal to the optic axis. The phase delay between these components leads to a change in the output polarization state. As an example, we will look at a retarder with a phase delay that equals π (= half-wave retarder) with an angle χ between the fast-axis and the linear polarization state. The output polarization state is also linear, but rotated by an angle $2\chi = \Phi$. Circularly polarized light travelling through the same half-wave retarder switches orientation such that left-circular polarization becomes right-circular polarization and vice versa, independent of fast-axis orientation. However, the phase of the output circular polarized light *is* dependent on the fast-axis orientation χ. The total phase delay of the circularly polarized light travelling through the half-wave plate is given by

$$\phi = \frac{2\pi n_{slow} d}{\lambda} \pm 2\chi. \tag{1.3}$$

The first part is the dynamic phase and is independent of the geometry of the optic axis, while the second part does depend on the orientation of the optic axis but is independent of wavelength. The second part is the geometric phase and also depends on the circular polarization state of the light coming in, where Φ is positive for left-circularly polarized light. If we compare the phase shift between circularly-polarized light with the same orientation travelling through the same retarder with a different orientation $\Delta\chi$, the phase *difference* is purely geometric phase.

$$\Delta\phi = \pm 2\Delta\chi = \pm\Delta\Phi. \tag{1.4}$$

A half-wave retarder with a fast-axis orientation pattern therefore is an optic that generates a phase pattern with a phase that is twice the angle of the fast-axis orientation pattern. Such an optic can also be called a geometric phase hologram (GPH), and has four important properties.

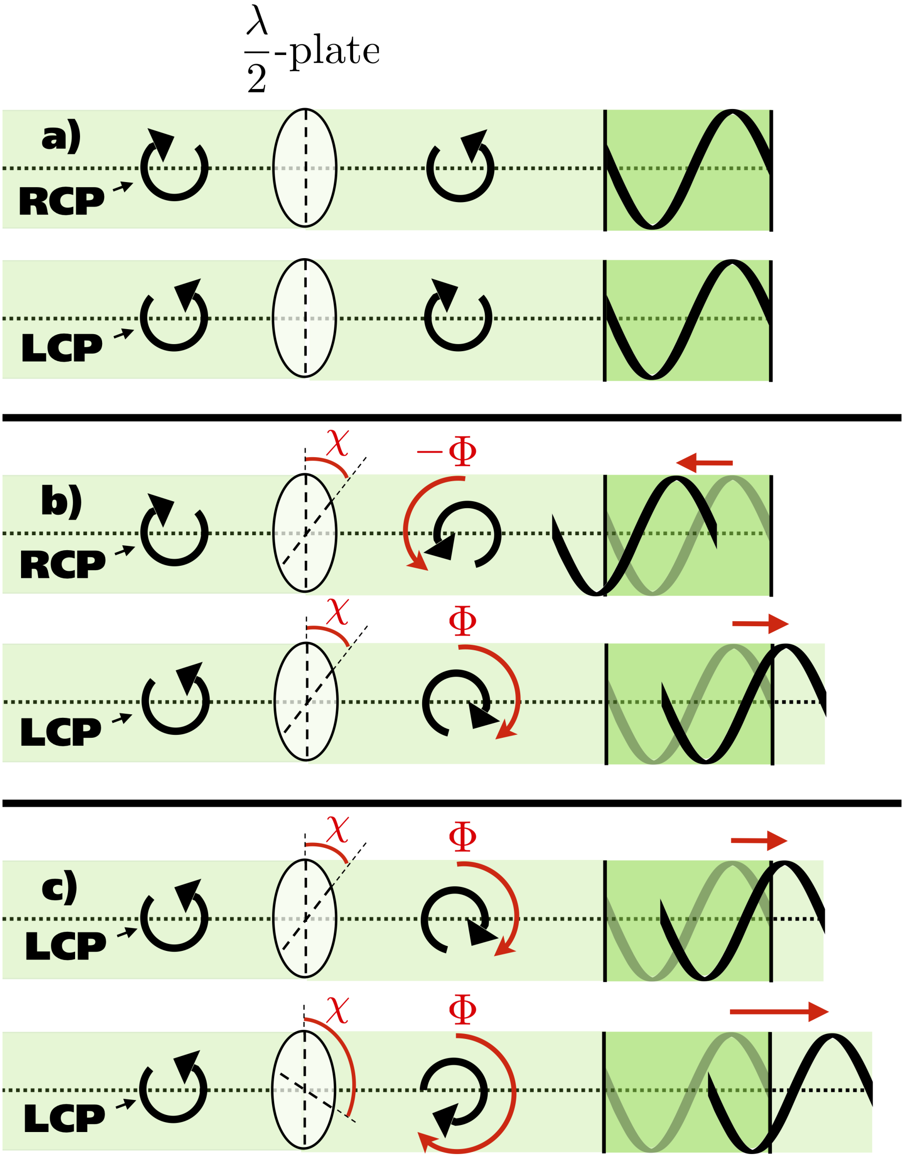

Figure 1.8: Properties of circularly polarized light passing through a half-wave retarder. **a)** Left-handed circularly polarized light (LCP) becomes right-handed circularly polarized light (RCP) and vice versa with a dynamical phase delay which we set as a reference. **b)** Rotating the half-wave retarder compared to the reference orientation results in an additional phase delay Φ called the geometric phase. The sign of the phase delay depends on the handedness of the incoming beam. **c)** The geometric phase shift Φ is plus or minus twice the rotation angle χ.

1. A GPH flips the circular polarization state.
2. The applied phase has an opposite sign for opposite handedness of the incoming circular polarization state.
3. A GPH applies geometric phase that only depends on the local fast-axis orientation and is therefore independent of wavelength.
4. When the retardance deviates from half-wave, the diffraction efficiency decreases and polarization leakage emerges.

A graphical representation of the first three properties is shown in Fig. 1.8 and Fig. 1.9. The fourth property can represent a major technical limitation, which is discussed in section 1.4.4

1.4.2 Geometric phase in the Jones formalism

To derive the properties of the geometric phase, we will have to describe polarized light in the Jones formalism. A beam of light that travels in the z-direction in Cartesian coordinates consists of an electric field that oscillates perpendicular to the z-direction. Decomposing this oscillation in the x-y plane results in the description of light in the Jones formalism (Born & Wolf, 2013), i.e.

$$\mathbf{E} = \begin{pmatrix} E_x \\ E_y \end{pmatrix} \tag{1.5}$$

If these components are in phase, the polarization state is linear, and the polarization state is circular if they are phase shifted by $\pi/2$ and have equal amplitude. Any other state is referred to as elliptical polarization, a combination of the linear and circular. Any optical element can then be written as a 2×2 Jones matrix and the Jones matrix of a linear retarder (LR) $\mathbf{J}_{\mathrm{LR}}$ is given by

$$\mathbf{J}_{\mathrm{LR}} = \begin{pmatrix} e^{i\phi_1} & 0 \\ 0 & e^{i\phi_2} \end{pmatrix}, \tag{1.6}$$

where $\phi_1 = \frac{2\pi}{\lambda} n_{\mathrm{o}} d$ and $\phi_2 = \frac{2\pi}{\lambda} n_{\mathrm{e}} d$. Here we assume that the optic axis is in the y-direction. The rotation matrix $\mathbf{J}_{\mathrm{rot}}(\chi)$ is given by

$$\mathbf{J}_{\mathrm{rot}}(\chi) = \begin{pmatrix} \cos\chi & \sin\chi \\ -\sin\chi & \cos\chi \end{pmatrix}. \tag{1.7}$$

The output Jones vector $\mathbf{E}_{\mathrm{out}}$ is then given by

$$\mathbf{E}_{\mathrm{out}} = \mathbf{J}_{\mathrm{rot}}(-\chi)\mathbf{J}_{\mathrm{LR}}\mathbf{J}_{\mathrm{rot}}(\chi)\mathbf{E}_{\mathrm{in},\pm} = \mathbf{J}\ \mathbf{E}_{\mathrm{in}} \tag{1.8}$$

For a half-wave plate $\phi_2 - \phi_1 = \pi(1 + 2 * n)$ with n an integer, and $\mathbf{J}$ becomes

$$\mathbf{J} = e^{i\phi_1} \begin{pmatrix} \cos\chi & -\sin\chi \\ \sin\chi & \cos\chi \end{pmatrix} \begin{pmatrix} 1 & 0 \\ 0 & e^{i(\phi_2 - \phi_1)} \end{pmatrix} \begin{pmatrix} \cos\chi & \sin\chi \\ -\sin\chi & \cos\chi \end{pmatrix} \tag{1.9}$$

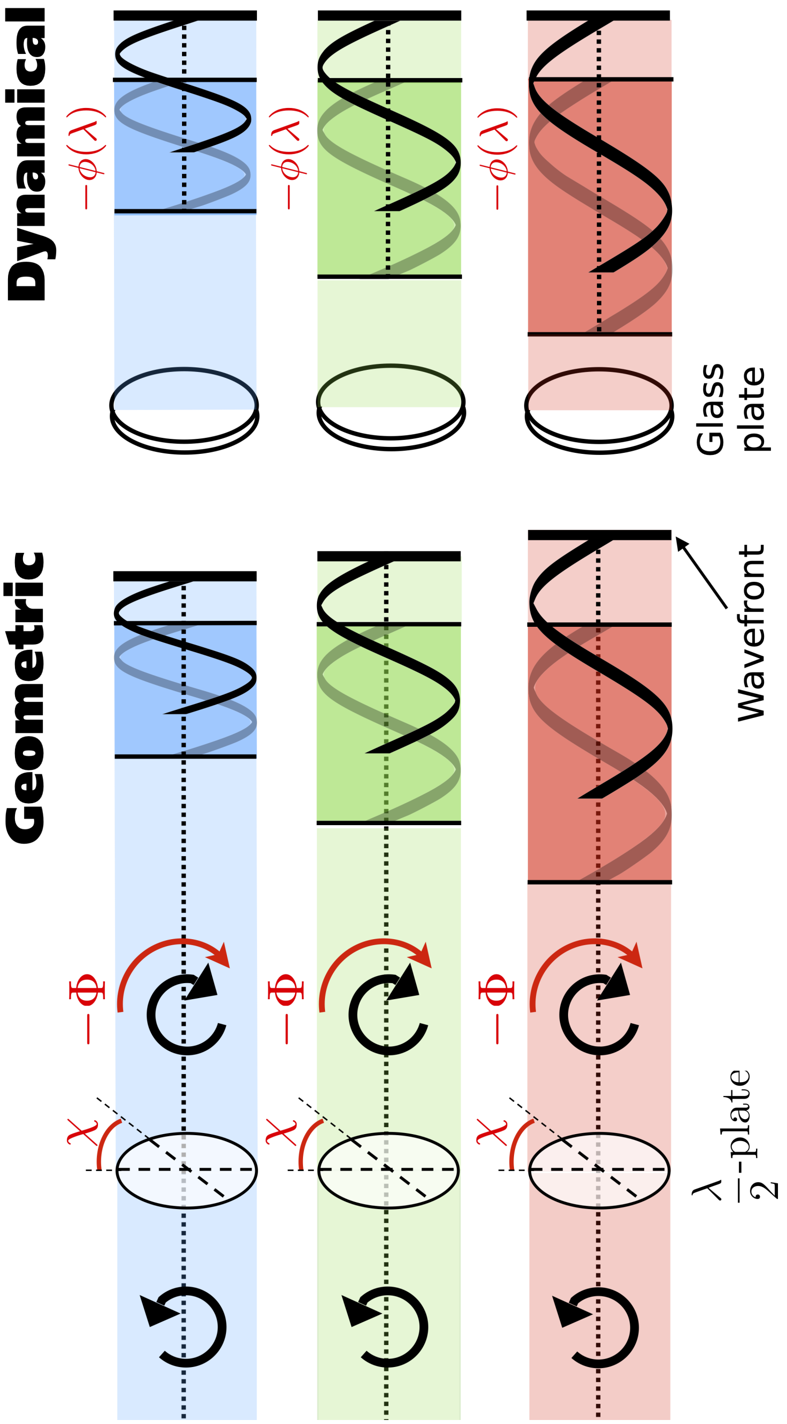

Figure 1.9: Comparison between the geometric phase and dynamical phase. The geometric phase shift is the same for each wavelength, while the dynamical phase shift is the same in terms of optical path length.

$$\mathbf{J} = e^{i\phi_1} \begin{pmatrix} \cos 2\chi & \sin 2\chi \\ \sin 2\chi & -\cos 2\chi \end{pmatrix} \tag{1.10}$$

Switching to the circular polarization basis reveals the beauty of the geometric phase for a rotating half-wave retarder (Mawet et al., 2009b):

$$\mathbf{J_{CP}} = e^{i\phi_1} \begin{pmatrix} 1 & i \\ 1 & -i \end{pmatrix} \begin{pmatrix} \cos 2\chi & \sin 2\chi \\ \sin 2\chi & -\cos 2\chi \end{pmatrix} \begin{pmatrix} 1 & i \\ 1 & -i \end{pmatrix}^{-1} = e^{i\phi_1} \begin{pmatrix} 0 & e^{2i\chi} \\ e^{-2i\chi} & 0 \end{pmatrix} . \tag{1.11}$$

For circularly polarized light the Jones vector in the circular polarization basis is given by

$$\mathbf{E}_{\text{in},LH} = \begin{pmatrix} 1 \\ 0 \end{pmatrix} \text{ and } \mathbf{E}_{\text{in},RH} = \begin{pmatrix} 0 \\ 1 \end{pmatrix} \tag{1.12}$$

From Eq. 1.11 and Eq. 1.12 the first three properties of a GPH are revealed:

$$\mathbf{E}_{\text{out}} = \mathbf{J_{CP}} \mathbf{E}_{\text{in},-} = e^{i\phi_1} \begin{pmatrix} 0 & e^{2i\chi} \\ e^{-2i\chi} & 0 \end{pmatrix} \begin{pmatrix} 0 \\ 1 \end{pmatrix} = e^{i(\phi_1 + 2\chi)} \begin{pmatrix} 1 \\ 0 \end{pmatrix} . \tag{1.13}$$

So we see that the circular polarization state is flipped, the geometric phase is opposite for opposite polarization states and phase only depends on the orientation of the fast axis when comparing the phase of two different orientations.

To derive what happens if the retardance is not half-wave we introduce a deviation from half-wave retardance ϵ, such that $\mathbf{J}$ becomes

$$\mathbf{J} = e^{i\phi_1} \begin{pmatrix} \cos\chi & -\sin\chi \\ \sin\chi & \cos\chi \end{pmatrix} \begin{pmatrix} 1 & 0 \\ 0 & e^{i(\pi+\epsilon)} \end{pmatrix} \begin{pmatrix} \cos\chi & \sin\chi \\ -\sin\chi & \cos\chi \end{pmatrix} . \tag{1.14}$$

In the circular polarization basis, the Jones matrix of the system is given by

$$\mathbf{J_{CP}} = c_V e^{i\phi_1} \begin{pmatrix} 0 & e^{2i\chi} \\ e^{-2i\chi} & 0 \end{pmatrix} + c_L e^{i\phi_1} \begin{pmatrix} 1 & 0 \\ 0 & 1 \end{pmatrix} , \tag{1.15}$$

where $c_V = \cos(\epsilon/2)$ and $c_L = \sin(\epsilon/2)$. The efficiency, defined as the fraction of intensity that acquires the geometric phase, is given by $|c_V|^2$ and depends only on the retardance. The fraction of intensity that does not acquire the geometric phase is called the *leakage term*, and is given by $|c_L|^2$. Also important to note is that the leakage term does not flip polarization states, resulting in the leakage term having the orthogonal circular polarization state as the main beam. This can be used for filtering the leakage term with circular polarizers (Mawet et al., 2010) or with polarization gratings as described in Chapter 4.

Another way of presenting polarized light is the Stokes formalism, where the light is represented by the Stokes vector:

$$\mathbf{E} = \begin{pmatrix} I \\ Q \\ U \\ V \end{pmatrix} , \tag{1.16}$$

where I is the total intensity of the beam, Q and U represent linearly polarized light with an oscillation in the 0° (x-direction) and 45° respectively, and V describes circularly polarized light. The total intensity $I \geq \sqrt{Q^2 + U^2 + V^2}$. For any degree of polarization, the polarization state can described by a vector in Q, U, V-space and a length of $\sqrt{Q^2 + U^2 + V^2}$. Objects that change the polarization state without depolarization, such as ideal retarders, change orientation of the vector by rotating it in the (Q,U,V) subspace of the 1+3 Hilbert space. All possible polarization states with the same length form a sphere in the Q, U, V-space, which is called the Poincaré sphere (Poincaré, 1892). This sphere is useful for a visual representation of the polarization state as the phase differences between the Jones vector components are represented by unique points on the sphere. The Poincaré sphere can also be used to visualize geometric phase.

1.4.3 A different look on geometric phase: a personal note

Whereas the creation of classical phase delays by optical path length differences is easily explained in text and figures, providing an intuitive explanation of geometric (Pancharatnam-Berry) phase is much harder. In literature, abstract descriptions are often presented, e.g. "A geometric-phase shift, by contrast, arises as a kind of 'memory' of the evolution of a lightwave through an anisotropic parameter space" (Escuti et al., 2016). While accurate, I found these explanations did not give me a good idea *how* geometric phase arises from geometry differences, just that it does. In the Jones formalism, mathematically the geometric phase emerges from the coordinate transformations of the Jones matrix given by the orientation of the half-wave retarder, but I did not find that much enlightening. As this thesis is centered around geometric phase, it is clear that this lack of a good explanation would be unacceptable. A clear description was formulated by Michael Berry himself (Berry, 1988):

"Take a pencil, lay it on the north pole of a globe and point it in the direction of any of the meridians: the lines of longitude that radiate from the pole. Move the pencil down along the line to the equator and, keeping it perpendicular to the equator, slide it to another line of longitude. Move the pencil back to the north pole along the new meridian, and you will find that although the pencil has been returned to its starting point and at no time was rotated, it no longer points along the original line of longitude."

This example clearly shows that the orientation of the pen depends only on the geometry of the circuit, not on the energy or mass of the pencil, or even its initial direction. However, it is seemingly disconnected to the geometric phase of half-wave retarders. This could not be further from the truth. It was the pioneering work of Shivaramakrishnan Pancharatnam that showed that geometric phase, polarization, and the area of closed curves on the Poincaré sphere are strictly connected (Pancharatnam, 1956). In fact, his work marks the start of the theory of geometric phase, which he measured almost 30 years before Michael Berry formalized the same theory for quantum mechanics. In his work, Pancharatnam used birefringent wave plates (= retarder) and a Mach-Zender interferometer to

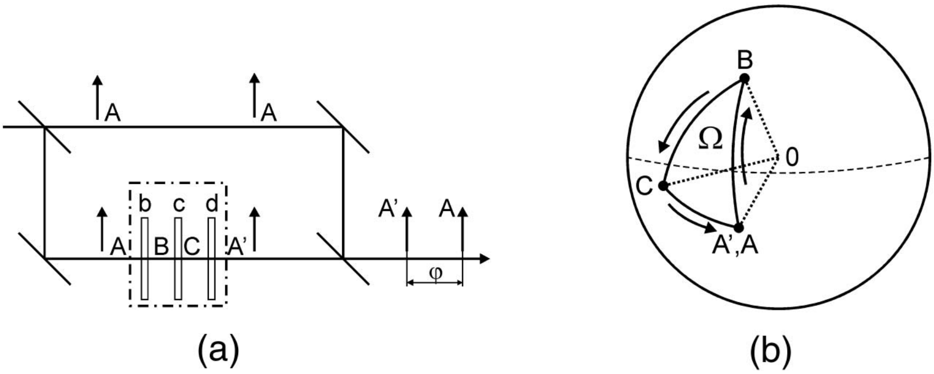

Figure 1.10: a) Set of birefringent media in a Mach-Zehnder setup and b) proper construction of the Pancharatnam's triangle to calculate the geometrical phase. From Kurzynowski et al. (2011).

investigate the interference between polarization states. His setup is described in Fig. 1.10 a), where he changed the polarization states of a second arm from input polarization **A**, to **B**, **C** and back to **A**', using the retarders *b*, *c* and *d*. Here, **A**' is identical to **A**, which is the unchanged polarization state of the first arm and the input. Pancharatnam showed that the second arm experiences a phase shift ϕ with respect to the first arm, and that the phase shift depends only the intermediate polarization states **B** and **C**, i.e. the history of **A**'. More importantly, he proved that this phase shift ϕ is equal to half the area (or steradian) of the geodesic triangle on the Poincaré sphere, Ω with the corners defined by the Stokes vectors of the polarization states **A**, to **B**, **C**. This geodesic triangle is shown in Fig. 1.10 b). The retarders are moving the polarization state by parallel transport or rotation on the surface of the Poincaré sphere, equivalent to the movement of the pen in the example of Berry.

The theory of Pancharatnam was later rediscovered for the rotation of the spin in quantum mechanics by Berry, who investigated (adiabatic) cyclic changes of quantum systems (Berry, 1984). For cyclic changes, by definition the output state is returned to the original state, like the polarization state in the experiment of Pancharatnam. This is different for half-wave retarders, where the output state is the opposite circular polarization state. So, how does this reconcile with the geometric phase arising from the cyclic change? For a single beam and a retarder, one can theoretically reconstruct a triangle using the wave plate's eigenwaves (Courtial, 1999) and reconstruct the dynamical phase and geometric phase from this triangle (Kurzynowski et al., 2011). However, conceptually easier is the interference between two beams, where a closed area on the Poincaré sphere can be formed if the two input and output polarization states are the same and their propagation distance is equal. This area is non-zero if each path experiences a different variation. For example, if the retarder *d* is flipped and moved from the second beam to the first, the output polarization states are **C** and **C**', with the same relative phase delay $\phi = \Omega/2$. The area does not necessarily have to form a closed triangle, other shapes are also possible if they form a closed area on the Poincaré sphere. This connects the half-wave retarders – with differently oriented fast-axis -flipping one circular polarization state to the other – to geometric phase, as is shown in Fig. 1.11 a). For a relative rotation of a half-wave axis, $\Delta\chi$, of a perfect half-wave retarder, the phase shift is $\Delta\Phi = 2\Delta\chi = 4\Omega$.

To summarize, the Poincaré sphere is a simple and effective visualization tool for the geometric (Pancharatnam) phase of light that is acquired when changing polarization states after being transmitted through an anisotropic medium. An identical visualization of the geometric (Berry) phase of adiabatically changing quantum systems can be made using the Bloch sphere (Bloch et al., 1946), which mathematically has the same properties. Another example is a sphere (unnamed) existing of Laguerre-Gaussian modes and Hermite-Gaussian modes of light (Padgett & Courtial, 1999; Alonso & Dennis, 2017), where also geometric phase accumulates for closed-loop transformations between these modes. The commonality of these examples is the angular momentum of the particles, that is circular polarization (= spin) and orbital angular momentum for photons and spin for the quantum systems. Photons have three different kinds of angular momentum, which are fundamentally connected through spin-orbit interactions and geometric phase (Bliokh et al., 2015). These spin-orbit interactions provide a theoretical frame work for many phenomenon in optics that are potentially interesting for high-contrast imaging systems. Examples are the spin-Hall effects in inhomogeneous media and at optical interfaces (e.g. the Imbert-Federov effect) (Bliokh & Aiello, 2013), and the interaction with subwavelength structures used for spin-controlled shaping of light, e.g. metasurfaces. Metasurfaces are a type of diffractive optics that are created with subwavelength features and enable pixelated control over the electric field and thus dynamic phase, polarization state, and geometric phase (Kildishev et al., 2013; Yu & Capasso, 2014). The term metasurface encompasses multiple types of subwavelength structures which modify the light based on different optical phenomenon (Huang et al., 2018). For example, dielectric metasurfaces realize dynamical phase differences with form birefringence, creating a local change in the refractive index with anisotropic subwavelength structures. Dielectric metasurfaces can also be used to generate geometric phase by rotating identical subwavelength structures (equivalent to liquid-crystal optics), or control both dynamical and geometric phase by changing both the structure shape and orientation (Rubin, 2020). Metallic metasurfaces are based on plasmonics, the interaction of light with a metallic interface, and they provide superior control of the light through spin-orbit interactions, e.g. surfaces with both polarization and wavelength dependent diffraction for simple polarimeters (Chen et al., 2016). Metasurfaces have a greater design freedom which could lead to new devices that can improve the performance of high-contrast imaging systems, much like the liquid-crystal devices in this thesis. Currently, metasurfaces with high diffraction efficiencies over large bandwidths can not be realized, and could face the same difficulties as stacks of independent patterned retarders (Mawet et al., 2006).

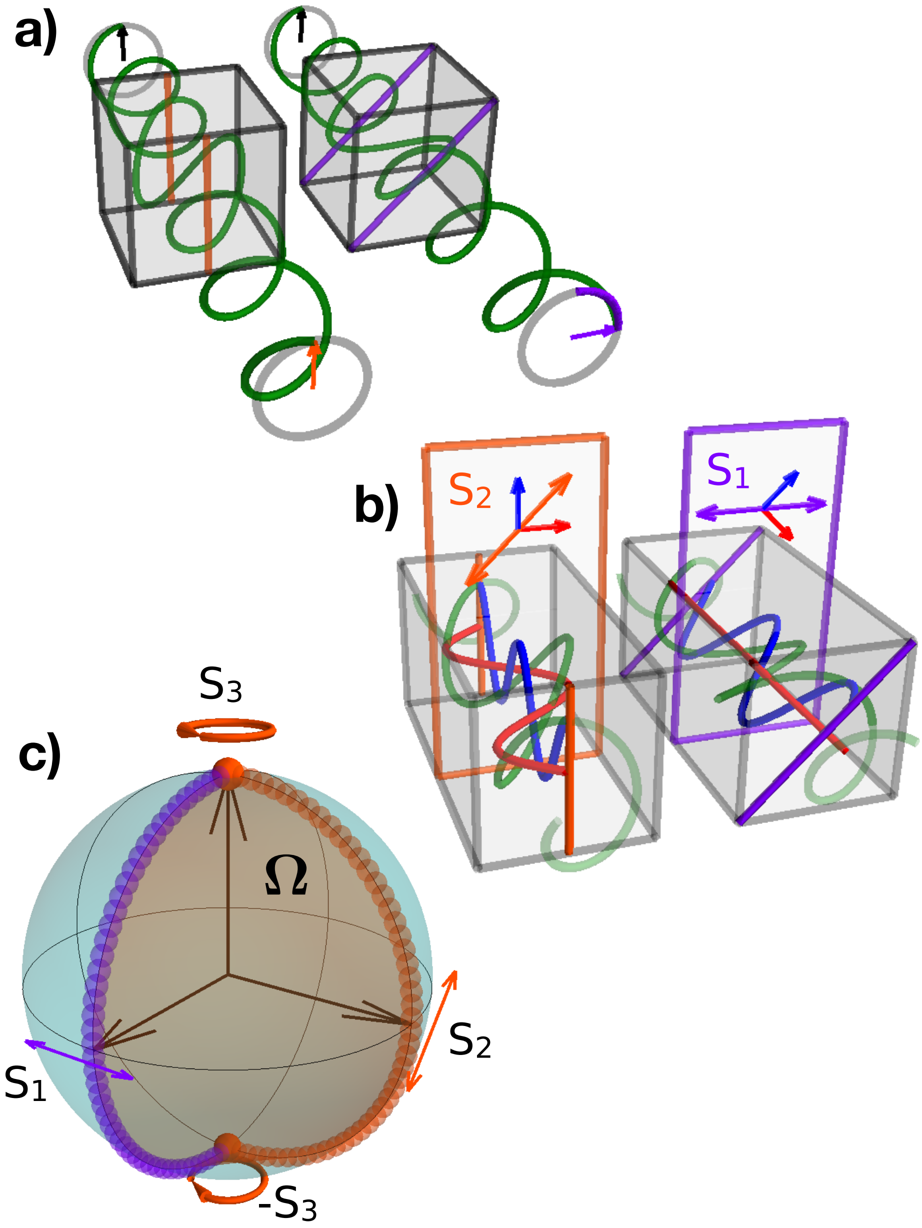

Figure 1.11: The effect of two neighbouring cells of a half-wave retarder with varying fast-axis orientations (0, 45°) on the incoming circularly polarized light. **a)** The resulting geometric phase represented by a phasor. **b)** The polarization states half-way through the same two cells, showing that the state depends on the fast-axis orientation. **c)** The closed curves on the Poincaré sphere with the area $\boldsymbol{\Omega}$ that is twice geometric phase, i.e. the area of a sphere is 4π and a quarter is π.

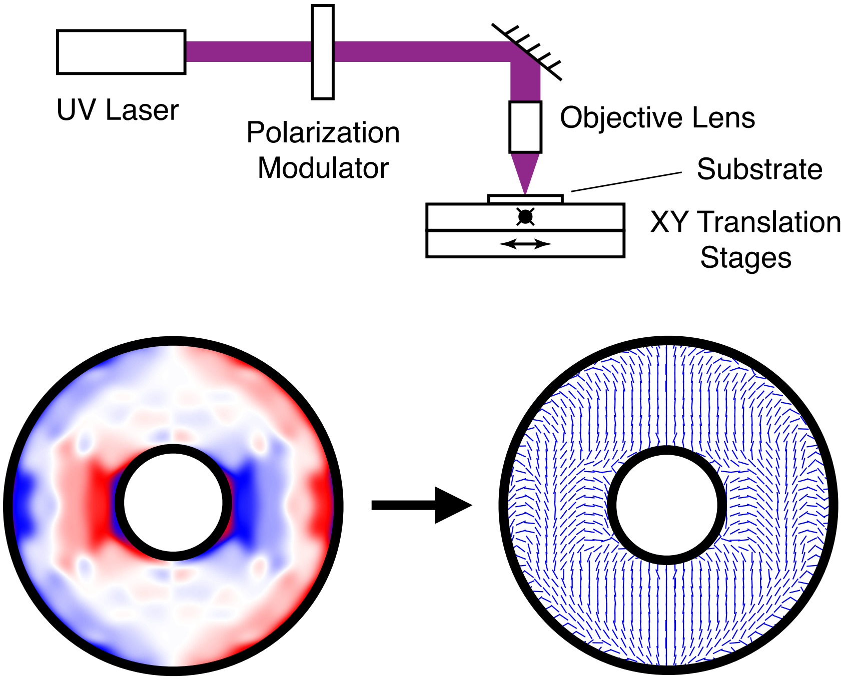

Figure 1.12: *Top:* Schematic of the direct-write system used to pattern a photo-alignment layer (PAL). The PAL records the orientation of incoming linearly-polarized UV radiation which is controlled by the polarization modulator. The substrate is translated to record arbitrary patterns. Adapted from Miskiewicz & Escuti (2014). *Bottom:* The phase pattern of a vAPP is encoded in the orientation of the fast axis of a half-wave retarder, and is written by the direct-write system. The phase pattern was used for the MagAO vAPP (Otten et al., 2017).

1.4.4 Technical implementation of a GPH

Theoretically, a geometric-phase hologram can be described as a half-wave retarder with a spatially varying fast-axis orientation. The technical implementation therefore will have to realize two important features. First, it needs to be capable of changing the fast-axis orientation as function of position. Second, it needs to have a half-wave retardance over a large bandwidth to ensure a small leakage term at all relevant wavelengths, especially to capitalize on the achromatic nature of the geometric phase. Liquid crystals are birefringent, so a thin layer can be used to create a zero-order half-wave plate. Patterning liquid crystals and achromatization are enabled by liquid-crystal technology. Creating arbitrary patterns is possible with a photo-alignment layer (PAL) (Chigrinov et al., 2008). Polymers in the PAL record the orientation of incoming linearly-polarized UV radiation, and direct-write laser scanning (Miskiewicz & Escuti, 2014; Kim et al., 2015) allows for accurately writing arbitrary patterns, An example of the direct-write system is shown in Fig. 1.12. As the geometric phase is twice the fast-axis orientation angle, the written pattern is half of the desired phase. With the high-precision translation stages and a small beam size, it is currently possible to accurately write phase patterns with a resolution down to $\sim 1\ \mu$m or cover an area up to 30×30 cm with a lower resolution. Therefore, the direct-write system enables the manufacturing of extreme phase patterns that can be required for vAPP coronagraphs or create vortex coronagraphs with extremely small central defects.

It was again Pancharatnam who first realized that achromatic retarders could be created with combinations of birefringent wave plates (Pancharatnam, 1955). Specifically, he showed with geometric arguments on the Poincaré sphere that a combination of three retarders, where the first and the last one have the same retardance and orientation, introduces a combined retardance that is similar over a larger wavelength range. The achromatization of phase plate coronagraphs started similarly, with the use of a two-stage stack of Quartz and MgF_2 for the four-quadrant phase-mask coronagraph (Mawet et al., 2006). Moreover, a three-stage stack was tried for the eight-octant phase-mask coronagraph manufactured with photonic crystals, which have periodic nanostructures with high and low refractive indices (Murakami et al., 2010, 2016). The form-birefringence of subwavelength structures can also be achromatized over 20% bandwidth, which has been used to create a vector-vortex coronagraph, i.e. the annular groove phase mask coronagraph (AGPM) (Mawet et al., 2005b; Catalán et al., 2016). A problem with a multi-stack is the alignment of the masks with respect to each-other, while the bandwidth of an AGPM is limited to 20%. Liquid crystals have a property that can be used to overcome these issues. The initial hologram orientation pattern in the PAL is passed on to the first and subsequent layers by *spontaneous self-alignment*. This way, liquid-crystal layers with different thickness and chiral twists may be arranged into a monolithic film (Komanduri et al., 2013). Another option is to combine materials with different refractive index (Schirmer & Schmidt-Kaler, 2000). The many degrees of freedom of these multi-twist retarder (MTR) films – given by the thickness and twist of each layer – may be used to tune the retardation of the liquid-crystal layer to half-wave retardance, achieving high efficiency (Kim et al., 2015; Escuti et al., 2016) in GPHs over large bandwidths into a single diffracted order. The tuning is an optimization problem that takes into account the physical constraints on the maximum twist to minimize the difference between the MTR retardance and half-wave retardance for a given wavelength range. An example of the monolithic structure of an MTR is shown in Fig. 1.13 a). Liquid-crystal MTRs can also be described on the Poincaré sphere, although their path is not a simple straight line on the surface. As MTRs are a combination of multiple birefringent liquid-crystal layers that act as separate retarders, each layer rotates the polarization on the Poincaré sphere. The combination of the layers can be manufactured to behave as a half-wave retarder, where the combined rotation is from one pole to the other for circularly polarized light, see Fig. 1.11 b). While the circuit on the surface of the Poincaré sphere is different for MTRs, the total area is the same as for a single half-wave retarder, resulting in the same geometric

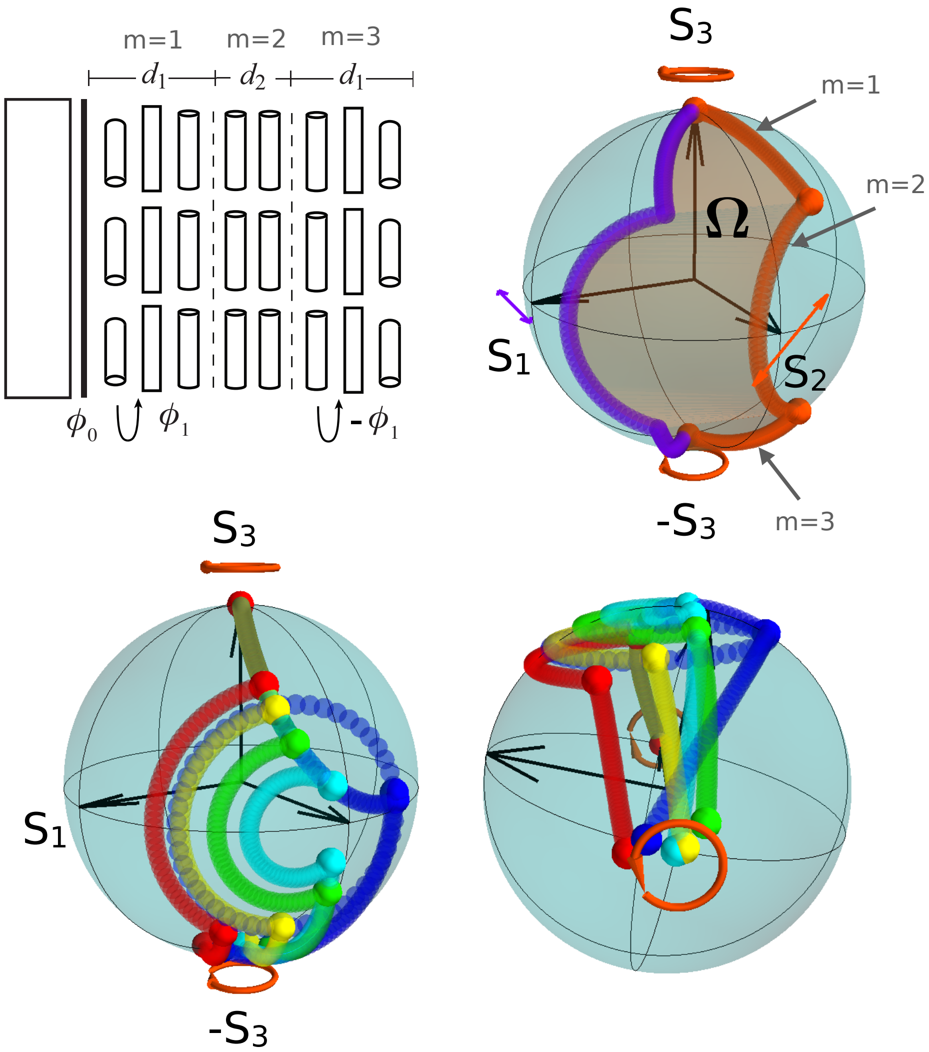

Figure 1.13: **a)** Illustration of the multi-twist retarder (MTR) monolithic structure, with one substrate and alignment layer, and three layers following a Pancharatnam design. The MTR design has a high efficiency ($> 97\%$) between 2-5 μm. Adapted from Komanduri et al. (2013). **b)** The closed curves on the Poincaré sphere of two MTRs with a fast-axis orientation of (0,30°). **c)** A side view and **d)** a bottom view of the curves of five different wavelengths on the Poincaré sphere, equally spaced between 2 μm (blue) and 5 μm (red).

phase. A single retarder has a wavelength dependent retardance, resulting in a different rotation on the Poincaré sphere for each wavelength. This principle holds for MTRs and can be used to optimize the recipe for close-to half-wave retardance over a large wavelength range. A Pancharatnam design for MTRs results in a first layer and third layer with the same thickness and an opposite twist, and a second layer with a different thickness and no twist. The chromatic behavior of such a design for a three-layer twist retarder is shown in Fig. 1.13.

With the direct-write and multi-twist retarder technologies it is possible to write any phase pattern with a high efficiency ($> 96\%$) over large bandwidths ($\delta\lambda/\lambda = 100\%$). Another advantage is the capability to write unbounded continuous phase while being completely flat. This advantage enables the increase of diffraction efficiencies for gratings, with up to 100% for a single order depending on the retardance. Such a liquid-crystal diffraction grating is called a polarization grating (PG), and has a continuously rotating fast-axis. A PG can also be described as a geometric phase prism because it constitutes a continuous phase ramp. Polarization gratings are diffractive polarization beam splitters due to the sign of the geometric phase changing with circular polarization state. The high efficiency, diffraction (= chromatic beam steering), and the polarization splitting property of PGs make them a versatile tool in optics. With the direct-write it is also possible to created shaped PGs, adding them to a phase pattern to separate polarization states or steering parts of a beam to different locations or indeed total freeform holograms. In this thesis, many applications of shaped PGs are discussed and how they can be used to overcome the challenges that come with the use of liquid-crystal technology. So far, we have not found an indication that the writing accuracy is not good enough for the applications in this thesis, so the main technological challenges are the minimization of the polarization leakage, the diffractive nature and for some applications the phase having the opposite sign for opposite circular polarization states. Polarization leakage limits the achieved contrast for many coronagraphs, e.g. vAPP and VVC, while the diffractive nature can be a problem for separating circular polarization states with PGs. The opposite sign of the phase reduces the planet throughput by a factor two for the vAPP and results in a diversity in aberrations between the two polarization states for the VVC (Riaud et al., 2012). One solution for the polarization leakage for the vAPP is adding a polarization grating pattern to the vAPP phase, i.e. the grating-vAPP (gvAPP) (Otten et al., 2014). However, this makes the vAPP diffractive and the planet light and stellar speckles are also diffracted, reducing the contrast. These examples clearly demonstrate some of the issues that occur when using liquid-crystal technology. In this thesis we present similar issues and, more importantly, how these can be solved by using more than one polarization grating.

1.5 This thesis

The goal of this thesis is to use the strengths of liquid-crystal technology to improve and integrate components of high-contrast imaging systems to facilitate detailed characterization of exoplanets. We use the extreme patterning and the inherently achromatic geometric phase to create optics that operate over large bandwidths, are more sensitive, or have additional capabilities. To this end, Chapter 2 of this work shows that liquid-crystal coronagraphs, such as the vAPP coronagraph, can be easily adapted to any coronagraphic system with good coronagraphic performance and summarize how it can be adapted for wavefront sensing or improving exoplanet photometry. Moreover, in Chapter 3 and 4 we demonstrate that improving the broadband performance of liquid-crystal coronagraphs is necessary to realize the full potential of integral field spectrographs and efficient exoplanet characterization. In Chapter 5 and 6 we enhance sparse aperture masking, capable of detecting companions beyond the diffraction limit, by using liquid-crystal phase masks to enable low-resolution spectroscopy and using most of the pupil. Both the liquid-crystal aperture mask and a vAPP with multiple gratings have gone through the complete development cycle, starting with the idea of a novel concept, to design, simulation, lab testing, on-sky verification, to science observations. In Chapter 7 we demonstrate that a broadband liquid-crystal version of the Zernike wavefront sensor can accurately and efficiently measure phase and amplitude aberrations simultaneously, facilitating extreme contrasts. The last Chapter, 8, describes a general method to efficiently modulate broadband light with independent phase control of orthogonal circular polarization states and wavelength bins.

Chapter 2: The vAPP coronagraph: creating dark holes in PSFs all over the world

The vector-Apodizing Phase Plate (vAPP) coronagraph is a versatile single-optic pupil-plane coronagraph that is easily adapted to any telescope aperture. Manufacturing vAPPs with the direct-write method for liquid-crystal technology enables extreme and accurate patterning and the multi-twist retarder technology provides excellent efficiencies ($> 96\%$) for bandwidths up to 100% between 0.55 μm and 5 μm. Furthermore, the vAPP is insensitive to tip-tilt errors, can easily be adapted to include focal-plane wavefront sensing capabilities, and can be designed with holographic off-axis PSFs that can be used as an astrometric and photometric reference. In this chapter, we report on the design, manufacturing, installation, verification, and the first on-sky results of seven different vAPPs in six different instruments. We give an overview of the different vAPPs and their instruments and explain their individual design choices. For all vAPPs we find that they are operating as expected by measuring PSF quality with the internal source of their respective instruments. We show how the data reduction of vAPPs and their D-shaped dark zone make observing and data reduction different from other coronagraphs and present preliminary software solutions. Lastly, we describe the designs of vAPPs baselined in future instruments, i.e. VLT/ERIS, ELT/METIS, and ELT/MICADO. Together, the vAPPs in these future instruments operate between 1.1 μm and 5 μm, and will provide high-resolution spectra ($R > 20,000$) of many already known, RV-detected planets, in addition to detecting and characterizing new planets.

Chapter 3: First low-resolution L-band spectroscopy of HR 8799 c,d,e with a LBT/ALES-vAPP combination.

In recent studies, both atmospheric modelling and IFS observations of directly imaged gas giants have focused on y-K band (0.9-2.5μm). However, observations of gas giants in the mid-infrared (3-5 μm) are critical to remove model degeneracies, determine their cloud properties, and give insight in their L-T transition. In this chapter, we report on the first on-sky results of the upgraded mid-infrared ALES spectrograph in combination with the newly installed vAPP coronagraph. This combination provides a unique window for exoplanet atmosphere studies, capable of providing low-resolution spectra between 2-5 μm using multiple instrument modes. We present HR 8799 observations with the ALES-vAPP combination using the L-band mode, spanning 2.8-4.2 μm with a spectral resolution of $\sim$ 35 representing the first mid-IR spectroscopy of HR8799 e. We employed a new observation strategy without nodding and only a limited amount of thermal background observations before and after, yielding an on-target observation efficiency of 93%. We detect all three HR 8799 planets in the field of view (HR 8799 c,d,e), becoming the first planets characterized with a vAPP coronagraph. In addition, we retrieve low-resolution spectra for all three planets between 3.5-4.1 μm, which are completely featureless and consistent with constant flux. The spectra of HR 8799 c, e are consistent with all previously reported photometric points, while HR 8799 d shows an unexplained increase in flux of 60%. However, all three spectra are consistent with previously reported Brα photometry (4.05 μm) of these planets. This is specifically interesting because most atmospheric models that use uniform clouds do not reproduce the flux at this wavelength, while rudimentary models of patchy clouds are more successful. Not only does this ALES-vAPP combination open a new spectroscopic window for exoplanets, it is also capable of time-variability studies enabled by the high observation efficiency and the presence of the stellar PSF. Based on the presented HR 8799 observations, the sensitivity would be $<\sim$ 5% per 1.5 hours of observing for all three planets, limited by the thermal background.

Chapter 4: Minimizing the effects of polarization leakage for liquid-crystal coronagraphs with multi-grating pattern combinations.

Currently, most ground-based coronagraphs have optimal performance in a single spectral band, while multi-band observations with integral field spectrographs (IFSs) are key to efficiently characterize exoplanets. In addition, the vector vortex coronagraph (VVC) is baselined for the HabEx mission, however, it does not reach the contrast requirement for the 20% bandwidth without extreme filtering of polarization leakage. In this chapter, we demonstrate that multi-grating pattern combinations can be used for liquid-crystal coronagraphs to suppress the polarization leakage by multiple orders of magnitude over a large bandwidth. This concept is different to other leakage minimization strategies because we use the patterning of separate liquid-crystal optics placed in succession to suppress leakage, rather than optimizing the retardance of the liquid-crystal layer itself. Using two polarization gratings composed of a single-layer liquid crystal structure in the lab, we demonstrate a leakage suppression of more than an order of magnitude over a bandwidth of 133 nm centered around 532 nm, compared to a single liquid-crystal optic. We also demonstrate a leakage suppression of three orders of magnitude at the center wavelength. Moreover, we apply the double-grating concept successfully to a VVC in the lab and a vAPP with an annular dark zone that is currently installed in LBT/LMIRcam. Simulations indicate that a combination of two multi-layered liquid-crystal PGs can suppress leakage to $< 10^{-5}$ for 1-2.5 μm. Such a double-grating VVC or vAPP would have optimal coronagraphic performance for the full bandwidth of a ground-based IFS, e.g. Subaru/CHARIS. In addition, we present simulations of a triple-grating solution that has $< 10^{-10}$ leakage on the first Airy ring from 450 to 800 nm for space-based applications. This triple-grating VVC would significantly relax the requirements of polarization leakage filtering, and can have a major impact on the system-level design and trade-offs, including the option to add spectroscopy and polarimetry.

Chapter 5&6: Multiplexed Holographic Aperture Masking with liquid-crystal geometric phase masks.

Sparse aperture masking (SAM) is an important technique to study processes like planet formation at solar-system scales. SAM is capable of characterizing structures down to half the diffraction limit and it produces observables that are resistant against wavefront aberrations, e.g. closure phases. However, it comes at the cost of a reduction in throughput, typically by 80-90%. In these two chapters we present holographic aperture masking (HAM), which aims at increasing the throughput of SAM by selectively combining all subapertures across a telescope pupil in multiple interferograms using a liquid-crystal phase mask, in addition to adding low-resolution spectroscopic capabilities. In Chapter 5 we show the principle of multiplexing, i.e. combining multiple phase ramps into a single phase pattern, in addition to designs and lab results of a technology demonstrator. In Chapter 6 we further develop the design with a complementary central (SAM) component and report on the design, construction and commissioning of a HAM prototype at the Keck OSIRIS Imager. We create a pipeline that extracts monochromatic closure phases from the central component as well as multi-wavelength closure phases from the holographic component. We test the performance of the HAM mask in the lab and on-sky, where we observed the binary star HDS 1507. We retrieve a constant separation of 120.9 ±0.5 mas for the independent wavelength bins, which is excellent agreement with literature values.

Combining the low-resolution spectra from observations in J, H, and K-band enables spectral characterization through spectral slopes which help distinguishing between scattered light and thermal signals.

Chapter 7: Simultaneous phase and amplitude aberration sensing with a liquid-crystal vector-Zernike phase mask.

Imaging Earth-like exoplanets in reflected light ($\sim 10^{-10}$ contrast), requires extremely sensitive, photon efficient phase and amplitude control with high spatial-frequency resolution. Similarly, ground-based instruments also require sensitive measurements of the wavefront to combat non-common path aberrations, which are currently limiting the achieved contrast at the smallest separations. The Zernike wavefront sensor (ZWFS) has these properties and therefore has recently been selected for the HabEx and LUVOIR missions. In this chapter we present an enhanced version of the ZWFS, the "vector-Zernike" wavefront sensor (vZWFS), which consists of a patterned liquid-crystal phase mask and optics to split circular polarization. The vZWFS extends the capabilities of the ZWFS, adding the capability to measure phase *and* amplitude aberrations *simultaneously.* We demonstrate reconstruction of the complex wavefront with monochromatic lab measurements and show in simulation the high accuracy and sensitivity over a bandwidth up to 100%, twice the bandwidth of a ZWFS. The advantages for future exoplanet missions are clear. Because the vZWFS measures the complex wavefront, it does not require amplitude calibration measurements, resulting in a more accurate reconstruction and a higher duty cycle. Moreover, the sensitivity over a large bandwidth increases the number of photons and consequently the reconstruction accuracy.

Chapter 8: Multi-color holography with a two-stage patterned liquid-crystal element.

The gvAPPs that are installed in many different instruments have two properties that are suboptimal for exoplanet imaging. Their grating is necessary to separate the left- and right-circular polarization states from each other and the leakage term, yet the dispersion smears planet light over many pixels, introducing more speckle and read noise. Secondly, the separation of circular polarization states directs half of the light in the bright-side of vAPP PSF, reducing the effective throughput by a factor of 2. More generally, the computer-generated geometric-phase holograms have wavelength-dependent output and cannot be used for the production of color imagery. In this chapter, we introduce a two-stage patterned liquid-crystal geometric phase hologram capable of producing white-light holograms. We implement a two-stage approach that first uses the wavelength-dependent diffraction to separate colors and circular polarization states, and second, directs these colors through separate holographic patterns. Moreover, by utilizing the geometric phase, we obtain diffraction efficiencies close to 100%. We successfully create a white light hologram from RGB input in the lab. In addition, we show in simulation how this two-stage element could be used for of true-color holograms. The two-stage GPH is directly portable for truly broadband vAPPs, free of polarization leakage and can be designed to have inner working angle that changes inversely wavelength. Likewise, the two-stage GPH provides direct control of both circular polarization states such that the D-shaped dark zone can be created on the same side.

1.6 Future Outlook

This thesis focuses on applications of liquid-crystal technology in high-contrast imaging (HCI) systems to implement any desired phase pattern in an achromatic and polarization-controlled fashion these systems. The fine resolution, achromatic nature and excellent efficiency of liquid-crystal geometric phase plates provides many opportunities to integrate multiple subsystems of HCI systems. As most applications have been developed during the last few years and have only been installed recently, they have not been used to their full potential.

1.6.1 A ground-based perspective

Ground-based telescopes have been the drivers of high-contrast imaging due to their large primary mirrors and the possibility to upgrade instruments. With the absence of competitive space-based high-contrast imaging systems until the launch of the Nancy Grace Roman Space Telescope (∼2025) (Roman, 2019), ground-based HCI is likely to continue to dominate the scientific discoveries from direct imaging the coming years. Large surveys from SPHERE and GPI are mostly completed, and have discovered less exoplanets than earlier models had predicted. Therefore, most efforts related to ground-based HCI are currently oriented towards developing and implementing new technology to improve the performance of existing HCI systems, i.e. achieving a better contrast at small inner working angles. Moreover, the lessons learned are implemented in first-generation instruments of the extremely large telescopes, which will open up a whole new parameter space in terms of IWA once these instruments are completed. Here we will describe how the work in this thesis will impact future observations and instruments.

Impact of broadband coronagraphs

Studies on coronagraph design have shown that phase-only masks have a better performance than amplitude masks (Mawet et al., 2009a; Por, 2017, 2020), and liquid crystals can be used to create arbitrary geometric phase patterns with high efficiencies. In addition, liquid-crystal optics can be tuned to operate from the visible to the infrared (0.55-5 μm), with a possible extension to from the UV to mid-infrared ($\sim$ 300 nm - 40 μm) (Packham et al., 2010). Applying this diversity to the vAPP in combination with the instantaneous wavelength coverage of more than an octave has an impact on the capabilities of multiple instruments. This is most relevant for instruments with an integral field spectrograph, observing with the full bandwidth instantaneously. A large advantage of this observing mode is that the coronagraphic performance is stable over the full wavelength range. In addition, spectral differential methods will benefit from the increased bandwidth. The first attempts of observing with a low-resolution (R=30) spectroscopic mode, using the full bandwidth of an integral field spectrograph, have been successful. Observations of HD 91312 with Subaru/SCExAO showed a constant coronagraphic performance for the full wavelength coverage of the CHARIS IFS. Moreover, the vAPPs installed in LBT/LMIRcam have provided the first mid-infrared spectrum of HR 8799 planets, see Chapter 3. While the spectrum is flat for gas giants with patchy clouds and a temperature above 1300K, cooler planets are expected to have transitioned to cloud free, CH_4-rich T-type atmospheres. Observations of these cooler planets, like 51 Eridani b, using the ALES spectrograph and the double-grating vAPP can constrain CH_4 content from the spectral slope between 3.5-4.1 μm. In addition, the contrast ratio for even cooler planets ($\sim$ 500 K) is most favorable in L or M (3-5 μm) band, providing good hunting grounds for LMIRcam imaging using the vAPP.

Another instrument that will benefit from the vAPP is the Magellan/MagAO-X system (Males et al., 2018), which provides an excellent AO performance in the visible. Compared to SPHERE/ZIMPOL, the AO system of MagAO-X will operate much faster (>3 kHz) and with more actuators on the deformable mirror (2K), resulting in a Strehl of 70% at Hα. Residual atmospheric tip-tilt aberrations do not result in a degradation of contrast because the vAPP is a pupil-plane coronagraph. Moreover, with the implementation of focal-plane wavefront sensing it is expected that the vAPP coronagraph will deliver unprecedented raw contrast ($< 10^{-3}$) at separation down to 50 mas. Accreting exoplanets like PDS 70 b and c will be prime targets for the Hα imaging mode of MagAO-X.

The VLT/ERIS instrument (Amico et al., 2012) will also become operational in the coming years, re-opening the mid-infrared window for the VLT after VLT/NACO was decommissioned. The imaging part of ERIS, NIX (Pearson et al., 2016), is equipped with a vAPP coronagraph (Boehle et al., 2018) that has been improved with respect the Magellan/MagAO vAPP (Otten et al., 2017) that is also operating in the Southern hemisphere. The ERIS instrument has two features that will help with the detection and characterization of new exoplanets. ERIS has a long-slit spectroscopic mode with a spectral resolution of $\sim$ 450 in L-band for non-coronagraphic imaging and the instrument has a visible wavefront sensor that can be fed by a laser guide star (Amico et al., 2012). Faint targets that were inaccessible with NACO can now be studied in great detail.

Components of the VLT/SPHERE instrument (Beuzit et al., 2019) will also be gradually upgraded in the coming years (Boccaletti et al., 2020), both for enhanced science as well as a roadmap towards a future dedicated high-contrast imaging system on the European Extremely Large Telescope (ELT), ELT/EPICS (Kasper et al., 2010). Equipped with a second-stage AO-system operating in the infrared and a medium-resolution integral field spectrograph, SPHERE will hunt for new exoplanets around fainter (lower mass) stars and characterize exoplanets in more detail. In addition, SPHERE will be able to perform high-resolution spectroscopy of gas giants with the HiRISE project (Vigan et al., 2018b), coupling SPHERE and CRIRES+ with a fiber. Both spectroscopic modes will benefit from an upgrade of the coronagraph under good observing conditions. While the liquid-crystal recipes for 100% bandwidth have only been applied for the vAPP, the vector vortex coronagraph can also benefit from the extended spectral bandwidth. A double-grating VVC of charge 2 with a pupil apodizer would provide excellent performance for the full SPHERE bandwidth ($0.9-2.5$ μm), with a theoretical inner working angle that is three times smaller than the most-used coronagraph.

Another coronagraph that is considered for SPHERE is an upgraded version of the current Apodized-Pupil Lyot Coronagraph (APLC) (Carbillet et al., 2011). A by-product of the creation of the vAPP optimizer was the proof that phase apodization always result in solutions with higher Strehl than amplitude apodization. Similarly, changing the pre-apodizer of the APLC to a phase apodizer, resulted in an improved performance for D-shaped dark zones. The Phase-Apodized-Pupil Lyot Coronagraph (PAPLC) with a knife-edge focal-plane mask yields inner working angles as close as 1.0 λ/D at contrasts of 10^{-10} with post-coronagraphic throughput up to 75% (Por, 2020). This coronagraph can be adapted to any pupil shape, which makes it ideal for segmented telescopes or telescopes with a non-zero central obscuration. A liquid-crystal phase plate implementation would extend the bandwidth of the PAPLC significantly, although this would require splitting of the opposite circular polarization states, similar to a gvAPP. The disadvantages are equivalent to a gvAPP, e.g. spectral smearing, D-shaped dark zone and losing factor two in planet throughput, see Chapter 2. Even so, the PAPLC had the best performance of all considered coronagraphs in simulations of a future SPHERE instrument and is therefore a prime candidate to replace the coronagraph (Boccaletti et al., 2020). Operating it in SPHERE will also be a first step to test these kinds of new technologies for ELT/EPICS.

With the five times larger primary mirror of ELT, it will be possible to detect fainter planets much closer in, down to solar system scales (<10 AU) for the nearest star forming regions. A first-generation ELT instrument is the AO assisted integral field spectrograph ELT/HARMONI (Thatte et al., 2016), which will provide R$\sim 500-20000$ resolution spectra for between 32000-8000 spaxels between 0.47-2.45 μm. Similar to VLT/MUSE and VLT/SINFONI, ELT/HARMONI can be used for direct imaging of exoplanets using the molecule-mapping technique. The other two first-generation instruments, ELT/METIS (Brandl et al., 2016) and ELT/MICADO (Davies et al., 2016), are capable of high-contrast imaging, have two and one vAPPs baselined respectively, and also have large bandwidths and spectroscopic capabilities (Kenworthy et al., 2018). Long-slit spectroscopy will provide modest spectral resolution for METIS (R~ 1500) in L and M band (3-5 μm), and good spectral resolution for MICADO (R $\sim 20,000$) in J, H, and K band (1-2.5 μm). METIS is also equipped with a high-resolution (R$\sim 100,000$) integral field spectrograph. The broadband capabilities of the vAPP are a good match with these modes, and the design of the vAPPs can easily be adapted to deliver good contrasts at small inner working angles despite the thick spiders and large central obscuration. Moreover, during the first years of operation both

instruments and the telescope will face unexpected difficulties that limit their performance. Especially vibrations will provide a challenge as the imaging resolution will increase a factor 5, while the mechanical structures have become much larger. Another challenge is the atmospheric dispersion, which will significantly impact MICADO where the focal-plane masks are in front of the atmospheric dispersion corrector (ADC). Because the coronagraphic performance of vAPPs are not sensitive to tip-tilt errors, the vAPP in MICADO will likely have an edge compared to other focal-plane coronagraphs. METIS has tip-tilt correction and an ADC, but residual tip-tilt and pointing drift will still significantly impact the performance (Carlomagno et al., 2020).
With the increased resolution, improved sensitivity and spectrographic capabilities of the first-generation of ELT instruments, it is expected that many new exoplanets will be directly imaged and characterized. The limitation of these instruments will be the performance of the adaptive-optics systems, which will not be good enough to directly image rocky exoplanets. ELT/EPICS, the second-generation instrument dedicated to high-contrast imaging, plans to capitalize on improved technology to open up this new parameter space (Kasper et al., 2010). The design of this instrument will depend on the lessons learned of technology demonstration projects like the SPHERE upgrades and the SCExAO and MagAO-X instruments. The instrument will have to be fully optimized on a system level, with hybrid coronagraphs, integrated focal-plane wavefront sensing, high-resolution spectroscopy, and polarimetry. Once completed, EPICS is expected to deliver 10^{-7}-10^{-8} post-processed contrast thanks to spectroscopy and/or polarimetry, which enables the detection and characterization of rocky planets in the habitable zone around the nearest M stars. EPICS will mainly observe planets previously found by indirect methods, characterizing the planet population by their atmospheric properties. Moreover, EPICS will have the spatial resolution necessary for imaging structures of a few AU at the nearest star-forming regions. EPICS will therefore be able to resolve snow lines in these regions and provide insight in their role in planet formation. In addition, EPICS enables the determination of the mass-luminosity relation for young gas giants, which also provides a rigorous test for planet formation models. Together with high-contrast imaging systems of the other ELTs, EPICS will provide fundamental insight in planet formation, disk-planet interaction and perhaps even habitability.

Benefits of a system approach

The freedom of the direct-write and multi-twist retarder technology for liquid-crystals also have enabled the integration between different subsystems in a HCI instrument. A first example is the possibility to add multiple PSF copies to the vAPP PSF, enabled only by the fine writing resolution. These holographic PSFs can be used as reference for the flux of companion PSFs, in addition to the coronagraphic PSF if it is not saturated, equivalent to Marois et al. (2006b) Flux variations that do not originate from companion variability, like a changing AO-performance with airmass, can be divided out. So far, the limits of this technique have not been investigated, but variations on the level of 1% could reveal the presence of clouds (Apai et al., 2013). These causes for companion variability are strongest in the near-infrared, and in the visible variability in H_α emission could provide insight in accretion mechanisms. At these wavelengths the AO-performance is more variable and using a vAPP is more beneficial.

Second, writing detailed patterns also enables holographic aperture masking (HAM), which provides spectrally-resolved closure phases and squared visibilities. Spectrally-resolved closure phases present a new observable for aperture masks used in imaging mode, and can be used to spectrally characterize targets down to 0.5 λ/D. Simultaneous spectral and spatial measurements can help constrain infrared spectral slopes, similar to the wavelength-dependent brightness ratio that is recovered for the binary HD 90823 in Chapter 6. The sensitivity that will be achieved by HAM is very dependent on the calibration of the closure phases and the polarization leakage. Currently, HAM in OSIRIS can determine wavelength-dependent brightness ratios with spectral resolutions of R=$6-15$ in J, H, and K band for binaries with contrast rations $\sim 10^{-1}$. With a future upgrade of the HAM optic, adding a double-grating, and an improved calibration strategy it will be possible to provide low-resolution spectra for objects higher contrasts ($< 10^{-2}$) down to $\sim$ 30 mas in H-band. For the ELTs the relative throughput of sparse aperture masks will be lower compared to an 8-m class telescope. The data reduction of SAM requires that the wavefront variations inside the individual holes should be minimal, resulting in a maximum hole size that depends on the coherence length of the atmosphere, not the mirror diameter. Segment gaps and phase steps from segmented telescopes are also a problem, and therefore holes in the aperture mask will be limited to a size on the order of a segment diameter. Moreover, many smaller non-redundant holes have a lower throughput than fewer larger ones. So, HAM would be an interesting way of improving the throughput. Unfortunately, the increase in the PSF size due to the smaller holes also reduces the spectral resolution, such that HAM on the ELT will likely be unable to spectrally resolve closure phases.

Combining high-contrast imaging systems with low-resolution spectroscopy has resulted in new insights in the atmospheres of gas giants, yet the gain in contrast by using the additional spectral information has been limited. This is different for medium- and high-resolution spectroscopy, where the raw-contrast of non-coronagraphic systems has been enhanced up to a factor 1000. The spectral differences between a star and its companion can be used to filter speckles and simultaneously characterize planets. With cross-correlation techniques of spectral templates it is possible to detect molecular features in the atmospheres of exoplanets (Snellen et al., 2010, 2015; Hoeijmakers et al., 2018a). Noise from the stellar PSF is limiting these retrievals, which suggests that using high-contrast imaging techniques could be beneficial. Adding a fiber in the focal plane to connect high-contrast imaging systems to high-resolution spectrographs is relatively straightforward, but it has an inner working angle that is limited by conventional coronagraph designs ($> 2\lambda/D$). A third integrated method resulted in two new concepts that have been developed with smaller inner working angles ($< 1\lambda/D$).

This integrated method works by creating a new type of coronagraph that uses the mode-filtering property of the single-mode fibers to suppress the starlight, i.e. Single-mode Complex Amplitude Refinement (SCAR) (Por & Haffert, 2020; Haffert et al., 2020) and Vortex Fiber Nulling (VFN) (Ruane et al., 2018). Both concepts change the shape the PSF with liquid-crystal phase masks in the pupil plane, such that locally the starlight has one or multiple nulls at the location of the fibers. These nulls do not contain the fundamental mode of the fibers, and high rejection ratios of 10^4 are achieved. SCAR is a direct descendant of the vAPP, optimizing a phase plate for different focal-plane constraints given by the fiber. The writing precision and the achromatic phase resulted in deep nulls over a 20% bandwidth, limited by the PSF scaling with wavelength. In addition, the first test version already benefited from the polarization grating to separate the leakage and the grating mask to create a pupil, two concepts developed for the vAPP. Both SCAR and the VFN would greatly benefit from the double-grating method to reduce the influence of polarization leakage. A double-grating version would remove the need for polarization filtering, increasing the efficiency of both by a factor of 2. The combination of these extreme inner working angles and high-spectral resolution will likely result in the detection and characterization of many planets, from rocky worlds to gas giants.

1.6.2 A space-based perspective

A long-term goal of high-contrast imaging is the detection and characterization of Earth-like exoplanets around solar-type stars. It is expected that ELTs will have the resolution and contrast to image rocky planets in the habitable zone around M-stars (Snellen et al., 2019). However, the extreme contrasts of such Earth-like planets in reflected light around solar-type stars, i.e. 10^{-10}, requires stabilization of the wavefront that can only achieved with space-based observatories. The technology demonstration for space-based systems have reached these contrast levels in lab conditions for small bandwidths, limited by chromatic bandwidths. It will take until the mid 2020s before the first technology demonstration mission is launched, i.e. the Nancy Grace Roman Space Telescope[6], and likely a decade thereafter before the current state of the art technology is operating in space.

As of yet, only the Hubble Space Telescope has some coronagraphic capabilities, although they are not competitive with ground-based results. Similarly, the James Webb Space Telescope will likely not outperform ground-based HCI systems in the visible and near-infrared, having an estimated instrumental wavefront error of 131 nm (Stahl, 2007). The performance of both NIRCam and MIRI will be limited by this wavefront aberration (Beichman et al., 2010; Boccaletti et al., 2015). It is likely that the post-processed performances will improve over time, as the extreme stability of space and low thermal background will help with improving the data reduction like with HST. We note that the stability is also beneficial for the non-redundant mask of NIRISS (2.7-5 mum), predicted to have a contrast of 10^{-5} between 60 and 500 mas (Sivaramakrishnan et al., 2010). While the contrast

---

[6] The Nancy Grace Roman Space Telescope was previously known as WFIRST

levels will be similar to ground-based, the unique wavelength coverage will provide new insights on disks through direct imaging and spectroscopy and close-in planets through transmission and secondary eclipse spectroscopy. Moreover, while the Roman Space Telescope will likely reach extreme contrasts of 10^{-8} and do amazing science, it is only a technology demonstrator for high-contrast imaging (Mennesson et al., 2020). These two aforementioned telescopes are part of the next-generation space telescopes, and are the only two with high-contrast imaging capabilities. Therefore, directly imaging Earth analogues will be out of reach for the coming decade. To fill this gap and to take advantage of the recent technology developments, two competing space missions have been proposed that have a large focus on the direct characterization of rocky Earth-like planets. These missions are HabEx (HabEx Study Team, 2019), a 4-m off-axis telescope and LUVOIR (LUVOIR Team et al., 2019), an 15-m (A) or 8-m (B) segmented telescope, both with a predicted launch date in 2035.

In preparation for these missions, the focus of space-based high-contrast imaging for the coming years is technology development and demonstration. Two key aspects that will ultimately determine the performance of these systems are wavefront sensing and coronagraphy. The challenges are to correct the wavefront with extreme precision, keeping it stable afterwards, and to manufacture coronagraphs that provide 10^{-10} contrast over a 20% bandwidth. The wavefront stability that is necessary for 10^{-10} contrast is 10 picometer RMS, putting stringent requirements on the wavefront sensor (Steeves et al., 2020). The wavefront sensor that has been selected for both HabEx and LUVOIR is a Zernike wavefront sensor (ZWFS), which is extremely sensitive, photon efficient, and has high spatial-frequency resolution. The geometric-phase version of the ZWFS, the vector-Zernike wavefront sensor (vZWFS), has several advantages compared of the ZWFS. The vZWFS is capable of reconstructing both phase and amplitude, does not require an amplitude calibration measurement and provides good reconstruction for larger bandwidths. These advantages would benefit the HabEx and LUVOIR missions and the vZWFS is therefore now being tested at the Jet Propulsion Laboratory, where they are investigating both a liquid-crystal version and a meta-material version. Moreover, the vZWFS is under study for implementation at the W. M. Keck Observatory.

The proposed coronagraphic systems of both HabEx and LUVOIR-B will make use of a vector-vortex coronagraph, where LUVOIR A and B will also be equipped with an apodized pupil Lyot coronagraph and a phase-induced amplitude apodization complex mask coronagraph. Liquid-crystal vector-vortex coronagraphs, however, do not reach the contrast requirement of $< 10^{-10}$ without extreme filtering of polarization leakage. Even with filtering, multiple VVCs will have to be installed to cover the full wavelength range of the coronagraphic instruments. A triple-grating vector-vortex coronagraph (tgVVC) can be manufactured to suppress the on-axis leakage by a factor of 10^{-8} over 100% bandwidth, resulting in $< 10^{-10}$ contrast at the inner working angle of a charge 6 vortex. For smaller bandwidths of $\sim 20\%$ a double-grating VVC will also provide enough leakage suppression. A charge 6 tgVVC with 1TR layers has been manufactured and will be tested in the near future in the test benches of the Jet Propulsion Laboratory. If these tests show that the tgVVC works as in simulation, a 100% bandwidth version can have a major impact on the system-level design. HabEx is now baselined with two arms in the visible, each with 40% bandwidth in two separate channels in the visible, spanning 0.45-0.67 μm (Blue channel) and 0.67-1.0 μm (Red channel). Another option that is considered uses a polarizing beam splitter to separate the two arms, enabling polarimetry. Both channels have a separate coronagraph, optimized for their respective wavelengths. A tgVVC would enable the creation of two identical arms which could be equipped with both blue and red filters, removing single-point failures. Moreover, a larger instantaneous bandwidth up to 50% is ideal for spectroscopy using single-mode fibers (Coker et al., 2019b,a). Lastly, the deformable mirrors of the two identical arms could be used to create complementary dark-hole shapes. So, a broadband coronagraph could significantly impact the instrument design.

The LUVOIR-B aperture with a central obscuration does not work well with the vortex coronagraph without pre-apodization. Another solution is the PAPLC, which was demonstrated to have the highest Earth-like exoplanet yield of all coronagraphs considered for LUVOIR-B. For small spectral bandwidths the weak phase apodization can easily be offloaded to the deformable mirrors of high-contrast imaging systems. Larger spectral bandwidths would require a liquid-crystal phase mask, like for SPHERE. Independent of the final implementation, the PAPLC and the tgVVC6 are prime candidates for next-generation space-based high-contrast imaging systems.

1.6.3 New applications of liquid-crystal technology for exoplanet detection

Besides the applications of liquid-crystal technology presented in this thesis and mentioned above, other new ideas or applications have been developed by our group and described in literature, some of which have been directly inspired by the work in this thesis. Here we will summarize these applications and discuss their impact.

The first application is the vector-speckle grid (Bos, 2020), which is closely related to the coronagraphic holograms used for photometric monitoring. The vector-speckle grid creates off-axis PSF copies that have both circular polarization states, rather than one as for the vAPP. Because the opposite polarization states have the opposite phase or amplitude modulation, they are instantaneously incoherent with the underlying halo and thus more stable. With liquid-crystal technology a vector-speckle grid is easily manufactured with high efficiency over large bandwidths, making them also ideal for spectroscopy.

Besides the vZWFS, liquid-crystal technology been used for improving upon other existing wavefront sensing methods. The liquid-crystal generalized optical differentiation wavefront sensor (Haffert, 2016) is more efficient than the other optical differentiation wavefront sensors, and it is possible to change the focal-plane amplitude modulation. A step function makes the wavefront sensor akin a pyramid wavefront sensor with extremely sharp edges (< 2 μm) for a lower price. Another type of wavefront sensor is the three-wave lateral shearing interferometer (TWLSI), which has extreme dynamic range and exquisite sensitivity. Commercial implementations of the TWLSI have low throughput due to inefficient gratings, which can be solved with liquid-crystal TWLSI. Combined with the wavelength ranges that liquid-crystal technology can provide, the TWLSI would prove to be an easy and efficient method for quality control of optical elements, or even serve as primary wavefront sensor in adaptive optics systems.

A completely different application of liquid-crystal technology has to do with precise astrometry for exoplanet detection. Detecting exoplanets with astrometry requires micro-arcsecond stability of an instrument. Effects like mechanical drifts or creep of optical surfaces create astrometric signals that overwhelm the signal of exoplanets. For instruments like ELT/MICADO, the instrument design is optimized to reduce any of these effects, increasing the cost and complexity of the instrument. The TOLIMAN space telescope (Bendek et al., 2018; Tuthill et al., 2018) has a radically different approach, using diffraction structures as astrometric ruler for differential astrometry of Alpha Centauri. Diffraction structures are interesting rulers as they are distorted the same way the objects are distorted. So rather than maximizing instrument stability, TOLIMAN creates a ruler that is immune to many of the errors that would drown the signal. Creating diffraction structures that form an astrometric grid is an optimization problem similar to the vAPP optimization, albeit with a less clear merit function. The grid is created using 0-π phase structures, and the pattern is optimized to create a regular grid of speckles with a homogeneous intensity. By using a liquid-crystal phase plate, it is also possible to add photometric reference holograms at the corners of the detector. These reference holograms create a small spectrum for spectral monitoring (R $\sim$ 500). A technology demonstrator mission called TinyTol employs such a liquid-crystal TOLIMAN optic and will be launched in a cubesat early 2021. The TOLIMAN project aims to launch a 30 cm telescope in the coming decade for the astrometric monitoring of Alpha Centauri A and B to look for Earth-like exoplanets in the habitable zone, which requires sub-microarcsecond astrometric metrology.

Finding an Earth-like exoplanet, or even finding biomarkers on these planets, does not equal finding life. Many proposed biomarkers can be generated by inorganic pathways, resulting in false positives when not carefully studied. Remote sensing of the only place known to harbour life, Earth, presents an opportunity to study what signals could present unbiased biomarkers. Instruments that observe an unresolved or partially resolved Earth will provide information that is similar to what future instruments will record for Earth-like exoplanets and will provide valuable benchmark spectra for radiative transfer codes used to model exoplanet spectra. Spectro-polarimetric measurements of Earth at different scattering angles can be used to infer the presence of liquid water oceans, clouds, and derive atmospheric properties. Moreover, they can give key insights in biomarkers, like O_2, the Chlorophyll Green Bump and the Vegetation Red Edge, and continuous monitoring can be used to detect continents and their specific features, like rain forests, deserts and ice caps (Stam, D. M., 2008; Klindžić et al., 2020). Perhaps even more interesting is spectro-polarimetry of circularly polarized light, which is likely an indicator of homo-chirality of life (Patty et al., 2019). Such spectro-polarimetric instruments are necessarily space-based, and could be placed on satellites or even on other celestial bodies. Without the need to resolve features using large optics, these instruments can be made very compact and without any moving parts. Two instruments in particular, LOUPE (Karalidi et al., 2012; Klindžić et al., 2020) and LSDpol (Snik et al., 2019), provide large spectral ranges and precision polarimetry in small volumes. One of the enabling technologies is the patterned liquid-crystal half-wave retarder, that is used to create the passive polarimetric modulation used for full-Stokes measurements with minimal diffraction. The work in this thesis on liquid-crystal recipes enables high broadband polarimetric efficiency for these instruments. It is likely that LOUPE will be installed on a Lunar lander, rover or orbiting mission, while LSDpol aims for installation on the ISS. We predict that their measurements are key to further our understanding the requirements for a remote detection of life.

Bibliography

Allard, F. 2013, Proceedings of the International Astronomical Union, 8, 271

Alonso, M. A., & Dennis, M. R. 2017, Optica, 4, 476

Amico, P., Marchetti, E., Pedichini, F., et al. 2012, in Ground-based and Airborne Instrumentation for Astronomy IV, Vol. 8446, International Society for Optics and Photonics, 844620

Apai, D., Radigan, J., Buenzli, E., et al. 2013, The Astrophysical Journal, 768, 121

Apai, D., Karalidi, T., Marley, M., et al. 2017, Science, 357, 683

Avenhaus, H., Quanz, S. P., Garufi, A., et al. 2018, The Astrophysical Journal, 863, 44

Balasubramanian, K., White, V. E., Yee, K. Y., et al. 2015, Journal of Astronomical Telescopes, Instruments, and Systems, 2, 011005

Baraffe, I., Chabrier, G., Barman, T. S., Allard, F., & Hauschildt, P. 2003, Astronomy & Astrophysics, 402, 701

Baraffe, I., Homeier, D., Allard, F., & Chabrier, G. 2015, Astronomy & Astrophysics, 577, A42

Barman, T. S., Konopacky, Q. M., Macintosh, B., & Marois, C. 2015, The Astrophysical Journal, 804, 61

Barman, T. S., Macintosh, B., Konopacky, Q. M., & Marois, C. 2011, The Astrophysical Journal, 733, 65

Baselmans, J. 2012, Journal of Low Temperature Physics, 167, 292

Beichman, C. A., Krist, J., Trauger, J. T., et al. 2010, Publications of the Astronomical Society of the Pacific, 122, 162

Bendek, E., Tuthill, P., Guyon, O., et al. 2018, in Space Telescopes and Instrumentation 2018: Optical, Infrared, and Millimeter Wave, Vol. 10698, International Society for Optics and Photonics, 106980G

Benz, W., Ida, S., Alibert, Y., Lin, D., & Mordasini, C. 2014, arXiv preprint arXiv:1402.7086

Berry, M. 1988, Scientific American, 259, 46

Berry, M. V. 1984, Proceedings of the Royal Society of London. A. Mathematical and Physical Sciences, 392, 45

Beuzit, J. L., Vigan, A., Mouillet, D., et al. 2019, arXiv preprint arXiv:1902.04080

Biller, B., Apai, D., Bonnefoy, M., et al. 2021, Monthly Notices of the Royal Astronomical Society

Bliokh, K. Y., & Aiello, A. 2013, Journal of Optics, 15, 014001

Bliokh, K. Y., Rodríguez-Fortuño, F. J., Nori, F., & Zayats, A. V. 2015, Nature Photonics, 9, 796

Bloch, F., Hansen, W., & Packard, M. 1946, Phys Rev, 70, 460

Boccaletti, A., Lagage, P.-O., Baudoz, P., et al. 2015, Publications of the Astronomical Society of the Pacific, 127, 633

Boccaletti, A., Chauvin, G., Mouillet, D., et al. 2020, arXiv preprint arXiv:2003.05714

Boehle, A., Glauser, A. M., Kenworthy, M. A., et al. 2018, in Ground-based and Airborne Instrumentation for Astronomy VII, Vol. 10702, International Society for Optics and Photonics, 107023Y

Bonnefoy, M., Zurlo, A., Baudino, J.-L., et al. 2016, Astronomy & Astrophysics, 587, A58

Born, M., & Wolf, E. 2013, Principles of optics: electromagnetic theory of propagation, interference and diffraction of light (Elsevier)

Bos, S. P. 2020, arXiv preprint arXiv:2005.08751

Bos, S. P., Doelman, D. S., Lozi, J., et al. 2019, A&A, 632, A48, doi: `10.1051/0004-6361/201936062`

Bowler, B. P., Liu, M. C., Dupuy, T. J., & Cushing, M. C. 2010, The Astrophysical Journal, 723, 850

Brandl, B. R., Agócs, T., Aitink-Kroes, G., et al. 2016, in Ground-based and Airborne Instrumentation for Astronomy VI, Vol. 9908, International Society for Optics and Photonics, 990820

Burgasser, A. J. 2014, arXiv preprint arXiv:1406.4887

Cantalloube, F., Por, E., Dohlen, K., et al. 2018, Astronomy & Astrophysics, 620, L10

Cantalloube, F., Farley, O., Milli, J., et al. 2020, Astronomy and Astrophysics-A&A

Carbillet, M., Bendjoya, P., Abe, L., et al. 2011, Experimental Astronomy, 30, 39

Carlomagno, B., Absil, O., Kenworthy, M., et al. 2016, in Adaptive Optics Systems V, Vol. 9909, International Society for Optics and Photonics, 990973

Carlomagno, B., Delacroix, C., Absil, O., et al. 2020, Journal of Astronomical Telescopes, Instruments, and Systems, 6, 035005

Carlotti, A., Mouillet, D., Correia, J.-J., et al. 2018, in Advances in Optical and Mechanical Technologies for Telescopes and Instrumentation III, Vol. 10706, International Society for Optics and Photonics, 107062M

Catalán, E. V., Huby, E., Forsberg, P., et al. 2016, Astronomy & Astrophysics, 595, A127

Charbonneau, D., Brown, T. M., Latham, D. W., & Mayor, M. 2000, ApJ, 529, L45, doi: `10.1086/312457`

Charnay, B., Bézard, B., Baudino, J.-L., et al. 2018, The Astrophysical Journal, 854, 172

Cheetham, A. C., Girard, J., Lacour, S., et al. 2016, in Optical and Infrared Interferometry and Imaging V, Vol. 9907, International Society for Optics and Photonics, 99072T

Chen, W. T., Török, P., Foreman, M. R., et al. 2016, Nanotechnology, 27, 224002

Chigrinov, V. G., Kozenkov, V. M., & Kwok, H.-S. 2008, Photoalignment of liquid crystalline materials: physics and applications, Vol. 17 (John Wiley & Sons)

Chilcote, J. K., Larkin, J. E., Maire, J., et al. 2012, in Ground-based and Airborne

Instrumentation for Astronomy IV, Vol. 8446, International Society for Optics and Photonics, 84468W

Chilcote, J. K., Bailey, V. P., De Rosa, R., et al. 2018, in Ground-based and Airborne Instrumentation for Astronomy VII, Vol. 10702, International Society for Optics and Photonics, 1070244

Claudi, R., Maire, A.-L., Mesa, D., et al. 2019, Astronomy & Astrophysics, 622, A96

Claudi, R. U., Turatto, M., Gratton, R. G., et al. 2008, in Ground-based and Airborne Instrumentation for Astronomy II, Vol. 7014, International Society for Optics and Photonics, 70143E

Codona, J. L., Kenworthy, M. A., Hinz, P. M., Angel, J. R. P., & Woolf, N. J. 2006, 6269, 62691N, doi: `10.1117/12.672727`

Coker, C. T., Sayson, J. L., Shaklan, S., et al. 2019a, in Techniques and Instrumentation for Detection of Exoplanets IX, Vol. 11117, International Society for Optics and Photonics, 111171A

Coker, C. T., Shaklan, S. B., Riggs, A. E., & Ruane, G. 2019b, Journal of Astronomical Telescopes, Instruments, and Systems, 5, 045003

Courtial, J. 1999, Optics communications, 171, 179

Currie, T., Burrows, A., Girard, J. H., et al. 2014, The Astrophysical Journal, 795, 133

Davies, R., Schubert, J., Hartl, M., et al. 2016, in Ground-based and Airborne Instrumentation for Astronomy VI, Vol. 9908, International Society for Optics and Photonics, 99081Z

De Boer, J., Langlois, M., Van Holstein, R. G., et al. 2020, Astronomy & Astrophysics, 633, A63

de Boer, J., Salter, G., Benisty, M., et al. 2016, A&A, 595, A114, doi: `10.1051/0004-6361/201629267`

De Kok, R., Stam, D., & Karalidi, T. 2011, The Astrophysical Journal, 741, 59

dit de la Roche, D. P., Hoeijmakers, H., & Snellen, I. 2018, Astronomy & Astrophysics, 616, A146

Escuti, M. J., Kim, J., & Kudenov, M. W. 2016, Optics & Photonics News, 27, 22

Fried, D. L. 1966, J. Opt. Soc. Am., 56, 1380, doi: `10.1364/JOSA.56.001380`

Fusco, T., Sauvage, J.-F., Mouillet, D., et al. 2016, in Adaptive Optics Systems V, Vol. 9909, International Society for Optics and Photonics, 99090U

Galicher, R., Baudoz, P., Rousset, G., Totems, J., & Mas, M. 2010, Astronomy & Astrophysics, 509, A31

Galicher, R., Baudoz, P., Delorme, J.-R., et al. 2019, A&A, 631, A143, doi: `10.1051/0004-6361/201936282`

Gauchet, L., Lacour, S., Lagrange, A.-M., et al. 2016, Astronomy & Astrophysics, 595, A31, doi: `10.1051/0004-6361/201526404`

Greenbaum, A. Z., Pueyo, L., Sivaramakrishnan, A., & Lacour, S. 2014, The Astrophysical Journal, 798, 68, doi: `10.1088/0004-637X/798/2/68`

Greenbaum, A. Z., Pueyo, L., Ruffio, J.-B., et al. 2018, The Astronomical Journal, 155, 226

Greenwood, D. P. 1977, JOSA, 67, 390

Groff, T. D., Kasdin, N. J., Limbach, M. A., et al. 2014, in Ground-based and Airborne Instrumentation for Astronomy V, Vol. 9147, International Society for Optics and Photonics, 91471W

Gull, S. F., & Skilling, J. 1984in , IET, 646–659

Guyon, O. 2005, ApJ, 629, 592, doi: `10.1086/431209`

Guyon, O., Pluzhnik, E. A., Galicher, R., et al. 2005, The Astrophysical Journal, 622, 744

HabEx Study Team. 2019, HabEx, Habitable Exoplanet Observatory, Tech. rep., Jet Propulsion Laboratory. `https://www.jpl.nasa.gov/habex/pdf/HabEx-Final-Report-Public-Release.pdf`

Haffert, S. 2016, Optics express, 24, 18986

Haffert, S., Bohn, A., de Boer, J., et al. 2019, Nature Astronomy, 3, 749

Haffert, S., Por, E., Keller, C., et al. 2020, Astronomy & Astrophysics, 635, A56

Haniff, C. A., Mackay, C., Titterington, D. J., et al. 1987, Nature, 328, 694

Hardy, J. W. 1998, Adaptive optics for astronomical telescopes, Vol. 16 (Oxford University Press on Demand)

Hartmann, J. 1900, Zeitschrift für Instrumentenkunde, 20, 47

Henry, G. W., Marcy, G. W., Butler, R. P., & Vogt, S. S. 2000, The Astrophysical Journal Letters, 529, L41

Hoeijmakers, H., Schwarz, H., Snellen, I., et al. 2018a, Astronomy & Astrophysics, 617, A144

Hoeijmakers, H. J., Ehrenreich, D., Heng, K., et al. 2018b, Nature, 560, 453

Högbom, J. 1974, Astronomy and Astrophysics Supplement Series, 15, 417

Howard, A. W., Sanchis-Ojeda, R., Marcy, G. W., et al. 2013, Nature, 503, 381

Huang, L., Zhang, S., & Zentgraf, T. 2018, Nanophotonics, 7, 1169

Huygens, C. 1698

Jensen-Clem, R., Mawet, D., Gonzalez, C. A. G., et al. 2017, The Astronomical Journal, 155, 19

Jovanovic, N., Schwab, C., Cvetojevic, N., Guyon, O., & Martinache, F. 2016, Publications of the Astronomical Society of the Pacific, 128, 121001

Jovanovic, N., Absil, O., Baudoz, P., et al. 2018, Review of high-contrast imaging systems for current and future ground-based and space-based telescopes: Part II. Common path wavefront sensing/control and coherent differential imaging, doi: `10.1117/12.2314260`

Karalidi, T., Stam, D., Snik, F., et al. 2012, Planetary and Space Science, 74, 202

Kasdin, N. J., Vanderbei, R. J., Spergel, D. N., & Littman, M. G. 2003, The Astrophysical Journal, 582, 1147

Kasper, M., Beuzit, J.-L., Verinaud, C., et al. 2010, in 1st AO4ELT conference-Adaptive Optics for Extremely Large Telescopes, EDP Sciences, 02009

Kenworthy, M. A., Absil, O., Carlomagno, B., et al. 2018, in Ground-based and Airborne Instrumentation for Astronomy VII, Vol. 10702, International Society for Optics and Photonics, 10702A3

Kenworthy, M. A., Codona, J. L., Hinz, P. M., et al. 2007, \Apj, 660, 762, doi: `10.1086/513596`

Kildishev, A. V., Boltasseva, A., & Shalaev, V. M. 2013, Science, 339

Kim, J., Li, Y., Miskiewicz, M. N., et al. 2015, Optica, 2, 958, doi: `10.1364/OPTICA.2.000958`

Kirkpatrick, J. D., Cushing, M. C., Gelino, C. R., et al. 2011, The Astrophysical Journal Supplement Series, 197, 19

Klindžić, D., Stam, D. M., Snik, F., et al. 2020, arXiv preprint arXiv:2007.16078

Komanduri, R. K., Lawler, K. F., & Escuti, M. J. 2013, Optics Express, 21, 404, doi: `10.1364/OE.21.000404`

Konopacky, Q., Marois, C., Macintosh, B., et al. 2016, The Astronomical Journal, 152, 28

Konopacky, Q. M., Barman, T. S., Macintosh, B. A., & Marois, C. 2013a, Science, 339, 1398, doi: `10.1126/science.1232003`

—. 2013b, Science, 339, 1398

Kreidberg, L., Bean, J. L., Désert, J.-M., et al. 2014, Nature, 505, 69

Kurzynowski, P., Woźniak, W. A., & Szarycz, M. 2011, JOSA A, 28, 475

Lacour, S., Tuthill, P., Amico, P., et al. 2011a, Astronomy & Astrophysics, 532, A72, doi: `10.1051/0004-6361/201116712`

Lacour, S., Tuthill, P., Ireland, M., Amico, P., & Girard, J. 2011b, The Messenger, 146, 18

Lacour, S., Nowak, M., Wang, J., et al. 2019, Astronomy & Astrophysics, 623, L11

Lafreniere, D., Marois, C., Doyon, R., Nadeau, D., & Artigau, É. 2007, The Astrophysical Journal, 660, 770

Lagrange, A.-M., Boccaletti, A., Langlois, M., et al. 2019, Astronomy & Astrophysics, 621, L8

Lavie, B., Mendonça, J. M., Mordasini, C., et al. 2017, The Astronomical Journal, 154, 91

Love, G. D. 1997, Applied optics, 36, 1517

Lozi, J., Guyon, O., Jovanovic, N., et al. 2018, in Adaptive Optics Systems VI, Vol. 10703, International Society for Optics and Photonics, 1070359

Lozi, J., Guyon, O., Jovanovic, N., et al. 2019, in 6th International Conference on Adaptive Optics for Extremely Large Telescopes, AO4ELT 2019

LUVOIR Team, et al. 2019, arXiv preprint arXiv:1912.06219

Lyot, B. 1939, Monthly Notices of the Royal Astronomical Society, 99, 580

Macintosh, B., Graham, J., Palmer, D., et al. 2006, in Advances in Adaptive Optics II, Vol. 6272, International Society for Optics and Photonics, 62720L

Macintosh, B., Graham, J. R., Barman, T., et al. 2015, Science, 350, 64, doi: `10.1126/science.aac5891`

Males, J. R., & Guyon, O. 2018, Journal of Astronomical Telescopes, Instruments, and Systems, 4, 019001

Males, J. R., Close, L. M., Miller, K., et al. 2018, Proc. SPIE

Marchis, F., Thibault, S., Côté, O., et al. 2018, AGUFM, 2018, P41C

Marley, M. S., Saumon, D., Cushing, M., et al. 2012, The Astrophysical Journal, 754, 135

Marois, C., Lafreniere, D., Doyon, R., Macintosh, B., & Nadeau, D. 2006a, ApJ, 641, 556

Marois, C., Lafreniere, D., Macintosh, B., & Doyon, R. 2006b, The Astrophysical Journal, 647, 612

Marois, C., Macintosh, B., Barman, T., et al. 2008, Science, 322, 1348

Marois, C., Zuckerman, B., Konopacky, Q. M., Macintosh, B., & Barman, T. 2010, Nature, 468, 1080

Martinez, P., Kasper, M., Costille, A., et al. 2013, Astronomy & Astrophysics, 554, A41

Martinez, P., Beaulieu, M., Barjot, K., et al. 2020, Astronomy & Astrophysics, 635, A126

Mawet, D., Pueyo, L., Moody, D., Krist, J., & Serabyn, E. 2010, Proc. SPIE, 7739, 773914, doi: `10.1117/12.858240`

Mawet, D., Pueyo, L., Moody, D., Krist, J., & Serabyn, E. 2010, in Modern Technologies in Space-and Ground-based Telescopes and Instrumentation, Vol. 7739, International Society for Optics and Photonics, 773914

Mawet, D., Riaud, P., Absil, O., & Surdej, J. 2005a, ApJ, 633, 1191, doi: `10.1086/462409`

—. 2005b, The Astrophysical Journal, 633, 1191

Mawet, D., Riaud, P., Baudrand, J., et al. 2006, Astronomy & Astrophysics, 448, 801

Mawet, D., Serabyn, E., Liewer, K., et al. 2009a, Optics Express, 17, 1902

—. 2009b, Optics express, 17, 1902, doi: `10.1364/OE.17.001902`

Mawet, D., Pueyo, L., Lawson, P., et al. 2012, ArXiv e-prints, 8442, 844204, doi: `10.1117/12.927245`

Mayor, M., & Queloz, D. 1995, Nature, 378, 355

Meeker, S. R., Mazin, B. A., Walter, A. B., et al. 2018, Publications of the Astronomical Society of the Pacific, 130, 065001

Mendillo, C. B., Hewawasam, K., Howe, G. A., et al. 2019, in Techniques and Instrumentation for Detection of Exoplanets IX, Vol. 11117, International Society for Optics and Photonics, 1111707

Mennesson, B., Juanola-Parramon, R., Nemati, B., et al. 2020, arXiv preprint arXiv:2008.05624

Metchev, S. A., Heinze, A., Apai, D., et al. 2015, The Astrophysical Journal, 799, 154

Miskiewicz, M. N., & Escuti, M. J. 2014, Optics Express, 22, 12691, doi: `10.1364/OE.22.012691`

Mollière, P., Stolker, T., Lacour, S., et al. 2020, Astronomy & Astrophysics, 640, A131

Murakami, N., Nishikawa, J., Akaiwa, N., et al. 2016, in Advances in Optical and Mechanical Technologies for Telescopes and Instrumentation II, Vol. 9912, International Society for Optics and Photonics, 99126G

Murakami, N., Nishikawa, J., Yokochi, K., et al. 2010, The Astrophysical Journal, 714, 772

N'Diaye, M., Fogarty, K., Soummer, R., et al. 2018, in Space Telescopes and Instrumentation 2018: Optical, Infrared, and Millimeter Wave, Vol. 10698, International Society for Optics and Photonics, 106986A

Nielsen, E. L., De Rosa, R. J., Macintosh, B., et al. 2019, The Astronomical Journal, 158, 13

Nowak, M., Lacour, S., Lagrange, A.-M., et al. 2020, A&A, 642, L2, doi: `10.1051/0004-6361/202039039`

Oppenheimer, B., Baranec, C., Beichman, C., et al. 2013, The Astrophysical Journal, 768, 24

Otten, G. P., Snik, F., Kenworthy, M. A., et al. 2014, in Advances in Optical and Mechanical Technologies for Telescopes and Instrumentation, Vol. 9151, International Society for Optics and Photonics, 91511R

Otten, G. P. P. L., Snik, F., Kenworthy, M. A., et al. 2017, ApJ, 834, 175, doi: `10.3847/1538-4357/834/2/175`

Packham, C., Escuti, M., Ginn, J., et al. 2010, PASP, 122, 1471, doi: `10.1086/657904`

Padgett, M. J., & Courtial, J. 1999, Optics letters, 24, 430

Pancharatnam, S. 1955, Proceedings of the Indian Academy of Sciences - Section A, XLI

—. 1956, Proceedings of the Indian Academy of Sciences - Section A, 44, 247, doi: `10.1007/BF03046095`

Patty, C. L., Ten Kate, I. L., Buma, W. J., et al. 2019, Astrobiology, 19, 1221

Pearson, D., Taylor, W., Davies, R., et al. 2016, in Ground-based and Airborne Instrumentation for Astronomy VI, Vol. 9908, International Society for Optics and Photonics, 99083F

Pérez, S., Casassus, S., Hales, A., et al. 2020, The Astrophysical Journal Letters, 889, L24

Perryman, M., Hartman, J., Bakos, G. Á., & Lindegren, L. 2014, The Astrophysical Journal, 797, 14

Petigura, E. A., Marcy, G. W., & Howard, A. W. 2013, The Astrophysical Journal, 770, 69

Poincaré, H. 1892, Théorie mathématique de la lumière II.: Nouvelles études sur la diffraction.–Théorie de la dispersion de Helmholtz. Leçons professées pendant le premier semestre 1891-1892, Vol. 1 (G. Carré)

Por, E., & Haffert, S. 2020, Astronomy & Astrophysics, 635, A55

Por, E. H. 2017, Proc. SPIE, 10400, 104000V

—. 2020, The Astrophysical Journal, 888, 127

Pueyo, L., Bailey, V., Bolcar, M., et al. 2019, BAAS, 51, 215

Radhakrishnan, V. M., Keller, C. U., & Doelman, N. 2018, in Adaptive Optics Systems VI, Vol. 10703, International Society for Optics and Photonics, 107034N

Ragazzoni, R. 1996, Journal of modern optics, 43, 289

Rajan, A., Rameau, J., De Rosa, R. J., et al. 2017, Astronomical Journal, doi: `10.3847/1538-3881/aa74db`

Riaud, P., Mawet, D., & Magette, A. 2012, Astronomy & Astrophysics, 545, A150

Roman, N. G. 2019, Annual Review of Astronomy and Astrophysics, 57, 1

Ruane, G., Jewell, J., Mawet, D., Pueyo, L., & Shaklan, S. 2016, in Advances in Optical and Mechanical Technologies for Telescopes and Instrumentation II, Vol. 9912, International Society for Optics and Photonics, 99122L

Ruane, G., Wang, J., Mawet, D., et al. 2018, The Astrophysical Journal, 867, 143

Ruane, G., Riggs, A., Mazoyer, J., et al. 2018, in Proc. Spie, Vol. 10698, doi: `10.1117/12.2312948`

Ruane, G., Ngo, H., Mawet, D., et al. 2019, The Astronomical Journal, 157, 118

Rubin, N. A. 2020, PhD thesis

Sallum, S., & Eisner, J. 2017, The Astrophysical Journal Supplement Series, 233, 9, doi: `10.3847/1538-4365/aa90bb`

Samland, M., Mollière, P., Bonnefoy, M., et al. 2017, A&A, 603, A57, doi: `10.1051/0004-6361/201629767`

Schirmer, J., & Schmidt-Kaler, T. 2000, Optics Communications, 176, 313

Seo, B.-J., Patterson, K., Balasubramanian, B., et al. 2019, in Techniques and Instrumentation for Detection of Exoplanets IX, Vol. 11117, International Society for Optics and Photonics, 111171V

Serabyn, E., Mawet, D., & Burruss, R. 2010, Nature, 464, 1018

Shack, R. V. 1971, J. Opt. Soc. Am., 61, 656

Shi, F., Cady, E., Seo, B.-J., et al. 2017, in Techniques and Instrumentation for Detection of Exoplanets VIII, Vol. 10400, International Society for Optics and Photonics, 104000D

Sing, D. K., Fortney, J. J., Nikolov, N., et al. 2016, Nature, 529, 59

Sissa, E., Gratton, R., Garufi, A., et al. 2018, Astronomy & Astrophysics, 619, A160

Sivaramakrishnan, A., Lafrenière, D., Tuthill, P. G., et al. 2010, in Space Telescopes and Instrumentation 2010: Optical, Infrared, and Millimeter Wave, Vol. 7731, International Society for Optics and Photonics, 77313W

Sivia, D. S. 1987, PhD thesis, University of Cambridge

Skemer, A. J., Hinz, P., Stone, J., et al. 2018, in Ground-based and Airborne Instrumentation for Astronomy VII, Vol. 10702, International Society for Optics and Photonics, 107020C

Skemer, A. J., Hinz, P. M., Esposito, S., et al. 2012, The Astrophysical Journal, 753, 14

Skemer, A. J., Marley, M. S., Hinz, P. M., et al. 2014, The Astrophysical Journal, 792, 17

Smith, B. A., & Terrile, R. J. 1984, Science, 226, 1421

Snellen, I., de Kok, R., Birkby, J., et al. 2015, Astronomy & Astrophysics, 576, A59

Snellen, I., Albrecht, S., Anglada-Escudé, G., et al. 2019, arXiv preprint arXiv:1908.01803

Snellen, I. A., Brandl, B. R., de Kok, R. J., et al. 2014, Nature, 509, 63

Snellen, I. A., De Kok, R. J., De Mooij, E. J., & Albrecht, S. 2010, Nature, 465, 1049

Snik, F., Otten, G., Kenworthy, M., et al. 2012, Proc. SPIE, 8450, 84500M, doi: `10.1117/12.926222`

Snik, F., Absil, O., Baudoz, P., et al. 2018, in , doi: `10.1117/12.2313957`

Snik, F., Keller, C. U., Doelman, D. S., et al. 2019, in Polarization Science and Remote Sensing IX, Vol. 11132, International Society for Optics and Photonics, 111320A

Soummer, R. 2004, The Astrophysical Journal Letters, 618, L161

Soummer, R., Hagan, J. B., Pueyo, L., et al. 2011a, The Astrophysical Journal, 741, 55

Soummer, R., Pueyo, L., & Larkin, J. 2012, The Astrophysical Journal Letters, 755, L28

Soummer, R., Sivaramakrishnan, A., Pueyo, L., Macintosh, B., & Oppenheimer, B. R. 2011b, The Astrophysical Journal, 729, 144

Sparks, W. B., & Ford, H. C. 2002, ApJ, 578, 543, doi: `10.1086/342401`

Stahl, H. P. 2007, in Optical Manufacturing and Testing VII, Vol. 6671, International Society for Optics and Photonics, 667102

Stam, D. M. 2008, A&A, 482, 989, doi: `10.1051/0004-6361:20078358`

Stark, C. C., Belikov, R., Bolcar, M. R., et al. 2019, Journal of Astronomical Telescopes, Instruments, and Systems, 5, 024009

Steeves, J., Wallace, J. K., Kettenbeil, C., & Jewell, J. 2020, Optica, 7, 1267

Stevenson, K. B., Désert, J.-M., Line, M. R., et al. 2014, Science, 346, 838

Stolker, T., Min, M., Stam, D. M., et al. 2017, Astronomy & Astrophysics, 607, A42

Stolker, T., Min, M., Stam, D. M., et al. 2017, A&A, 607, A42, doi: `10.1051/0004-6361/201730780`

Su, K., Rieke, G., Stapelfeldt, K., et al. 2009, The Astrophysical Journal, 705, 314

Thatte, N. A., Clarke, F., Bryson, I., et al. 2016, in Ground-based and Airborne Instrumentation for Astronomy VI, Vol. 9908, International Society for Optics and Photonics, 99081X

Traub, W. A., & Oppenheimer, B. R. 2010, in Exoplanets (University of Arizona Press, Phoenix), 111–156, doi: `10.1098/rsta.2013.0090`

Trauger, J. T., Moody, D. C., Krist, J. E., & Gordon, B. L. 2016, Journal of Astronomical Telescopes, Instruments, and Systems, 2, 011013

Tuthill, P., Monnier, J., Danchi, W., Wishnow, E., & Haniff, C. 2000, Publications of the Astronomical Society of the Pacific, 112, 555

Tuthill, P., Lloyd, J., Ireland, M., et al. 2006, in Advances in Adaptive Optics II, Vol. 6272, International Society for Optics and Photonics, 62723A

Tuthill, P., Bendek, E., Guyon, O., et al. 2018, in Optical and Infrared Interferometry and Imaging VI, Vol. 10701, International Society for Optics and Photonics, 107011J

Tuthill, P. G., Monnier, J. D., & Danchi, W. C. 1999, Nature, 398, 487, doi: `10.1038/19033`

van Holstein, R., Stolker, T., Jensen-Clem, R., et al. 2021, Astronomy & Astrophysics

van Holstein, R. G., Snik, F., Girard, J. H., et al. 2017, in Techniques and Instrumentation for Detection of Exoplanets VIII, Vol. 10400, International Society for Optics and Photonics, 1040015

Van Holstein, R. G., Girard, J. H., De Boer, J., et al. 2020, Astronomy & Astrophysics, 633, A64

van Kooten, M., Doelman, N., & Kenworthy, M. 2019, JOSA A, 36, 731

Vigan, A., N'Diaye, M., Dohlen, K., et al. 2018a, in Adaptive Optics Systems VI, Vol. 10703, International Society for Optics and Photonics, 107035O

Vigan, A., Otten, G., Muslimov, E., et al. 2018b, in Ground-based and Airborne Instrumentation for Astronomy VII, Vol. 10702, International Society for Optics and Photonics, 1070236

Vigan, A., Fontanive, C., Meyer, M., et al. 2020, arXiv preprint arXiv:2007.06573

Vos, J. M., Allers, K., Apai, D., et al. 2019, arXiv preprint arXiv:1903.06691

Wang, J., Mawet, D., Ruane, G., Hu, R., & Benneke, B. 2017, The Astronomical Journal, 153, 183

Wang, J., Wang, J. J., Ma, B., et al. 2020, The Astronomical Journal, 160, 150

Wang, J. J., Graham, J. R., Dawson, R., et al. 2018, The Astronomical Journal, 156, 192

Wilby, M. J., Keller, C. U., Snik, F., Korkiakoski, V., & Pietrow, A. G. M. 2017, A&A, 597, A112, doi: `10.1051/0004-6361/201628628`

Wolszczan, A., & Frail, D. A. 1992, Nature, 355, 145

Yeh, P. 2007, in 2007 Conference on Lasers and Electro-Optics-Pacific Rim, IEEE, 1–1

Yu, N., & Capasso, F. 2014, Nature materials, 13, 139

Zhou, Y., Apai, D., Bedin, L. R., et al. 2020, The Astronomical Journal, 159, 140

Zurlo, A., Vigan, A., Galicher, R., et al. 2016, Astronomy and Astrophysics, 587, A57, doi: `10.1051/0004-6361/201526835`